

# Tectonics

## RESEARCH ARTICLE

10.1029/2018TC005379

### Key Points:

- Seismicity data are used to probe crust and upper mantle structure and to evaluate fault kinematics in the southern Tanganyika rift
- Brittle strain is localized to steep border faults that penetrate to 25- to 40-km depth based on earthquake distribution and focal mechanisms
- Thick seismogenic layer and isolated swarms of upper mantle earthquakes indicate that  $M > 7$  earthquakes are probable

### Supporting Information:

- Supporting Information S1
- Table S1

### Correspondence to:

A. Lavayssière,  
aude.lavayssiere@noc.soton.ac.uk

### Citation:

Lavayssière, A., Drooff, C., Ebinger, C., Gallacher, R., Illsley-Kemp, F., Oliva, S. J., & Keir, D. (2019). Depth extent and kinematics of faulting in the southern Tanganyika rift, Africa. *Tectonics*, 38, 842–862. <https://doi.org/10.1029/2018TC005379>







Received 30 OCT 2018

Accepted 30 JAN 2019

Accepted article online 3 FEB 2019

Published online 2 MAR 2019

## Depth Extent and Kinematics of Faulting in the Southern Tanganyika Rift, Africa

Aude Lavayssière<sup>1</sup> , Connor Drooff<sup>2</sup>, Cynthia Ebinger<sup>3</sup> , Ryan Gallacher<sup>1,3</sup> , Finnigan Illsley-Kemp<sup>1,4</sup> , Sarah J. Oliva<sup>3</sup> , and Derek Keir<sup>1,5</sup> 

<sup>1</sup>Ocean and Earth Science, National Oceanography Centre Southampton, University of Southampton, Southampton, UK, <sup>2</sup>Department of Earth and Environmental Sciences, Michigan State University, East Lansing, MI, USA, <sup>3</sup>Department of Earth and Environmental Sciences, Tulane University, New Orleans, LA, USA, <sup>4</sup>School of Geography, Environment and Earth Sciences, Victoria University of Wellington, Wellington, New Zealand, <sup>5</sup>Dipartimento di Scienze della Terra, Università degli Studi di Firenze, Florence, Italy

**Abstract** Unusually deep earthquakes occur beneath rift segments with and without surface expressions of magmatism in the East African Rift system. The Tanganyika rift is part of the Western rift and has no surface evidence of magmatism. The TANG14 array was deployed in the southern Tanganyika rift, where earthquakes of magnitude up to 7.4 have occurred, to probe crust and upper mantle structure and evaluate fault kinematics. Four hundred seventy-four earthquakes detected between June 2014 and September 2015 are located using a new regional velocity model. The precise locations, magnitudes, and source mechanisms of local and teleseismic earthquakes are used to determine seismogenic layer thickness, delineate active faults, evaluate regional extension direction, and evaluate kinematics of border faults. The active faults span more than 350 km with deep normal faults transecting the thick Bangweulu craton, indicating a wide plate boundary zone. The seismogenic layer thickness is 42 km, spanning the entire crust beneath the rift basins and their uplifted flanks. Earthquakes in the upper mantle are also detected. Deep earthquakes with steep nodal planes occur along subsurface projections of Tanganyika and Rukwa border faults, indicating that large offset ( $\geq 5$  km) faults penetrate to the base of the crust, and are the current locus of strain. The focal mechanisms, continuous depth distribution, and correlation with mapped structures indicate that steep, deep border faults maintain a half-graben morphology over at least 12 Myr of basin evolution. Fault scaling based on our results suggests that  $M > 7$  earthquakes along Tanganyika border faults are possible.

## 1. Introduction

From inception, rift zones show a regular along-axis structural segmentation into basins bounded on one or both sides by large offset border faults. Border faults have the largest dimensions of the fault populations, they accommodate a large percentage of brittle extensional strain, and they are sites of potentially damaging earthquakes (e.g., Camelbeeck & Iranga, 1996; Ebinger et al., 1999; Jackson & Blenkinsop, 1993). Where rifting initiates in thick, strong cratonic lithosphere, the border fault throw is commonly larger than the heave, leading to fault dips greater than  $45^\circ$ . Flexural compensation results in 5- to 7-km-deep sedimentary basins bounded by uplifted flanks that may rise 3 km above the surrounding topography (e.g., Ebinger et al., 1999; Wannamaker et al., 2017). The broad, tall flanks and wide, deep basins can be explained by elastic or rheologically layered models of mechanically strong lithosphere with crustal-scale border faults (e.g., Watts & Burov, 2003; Weissel & Karner, 1989). Yet questions remain regarding the distribution and kinematics of faulting in the lower crust and upper mantle, the time evolution of strain, and the implications for earthquake hazards in rift zones. Earthquake focal mechanisms from active continental rift zones provide snapshots of fault kinematics and provide important constraints on the rheology of the old, cold continental plates over the time scales of the earthquake cycle (e.g., Yang & Chen, 2010).

The Tanganyika rift zone (Figure 1), East Africa, is one of the most seismically active sectors of the East African Rift system, hosting earthquakes from the surface to at least 39 km, as detected at teleseismic distances (e.g., Craig et al., 2011; Shudofsky, 1985; Yang & Chen, 2010; Figure 2 and Table S1 in the supporting information). The largest African earthquake ( $M$  7.4) occurred in 1910 beneath the Rukwa basin (Ambraseys & Adams, 1992). The nearest permanent station is the GSN station in Uganda, and there is no regional network that encompasses this study area. These gaps, as well as the possibility for very large earthquakes,

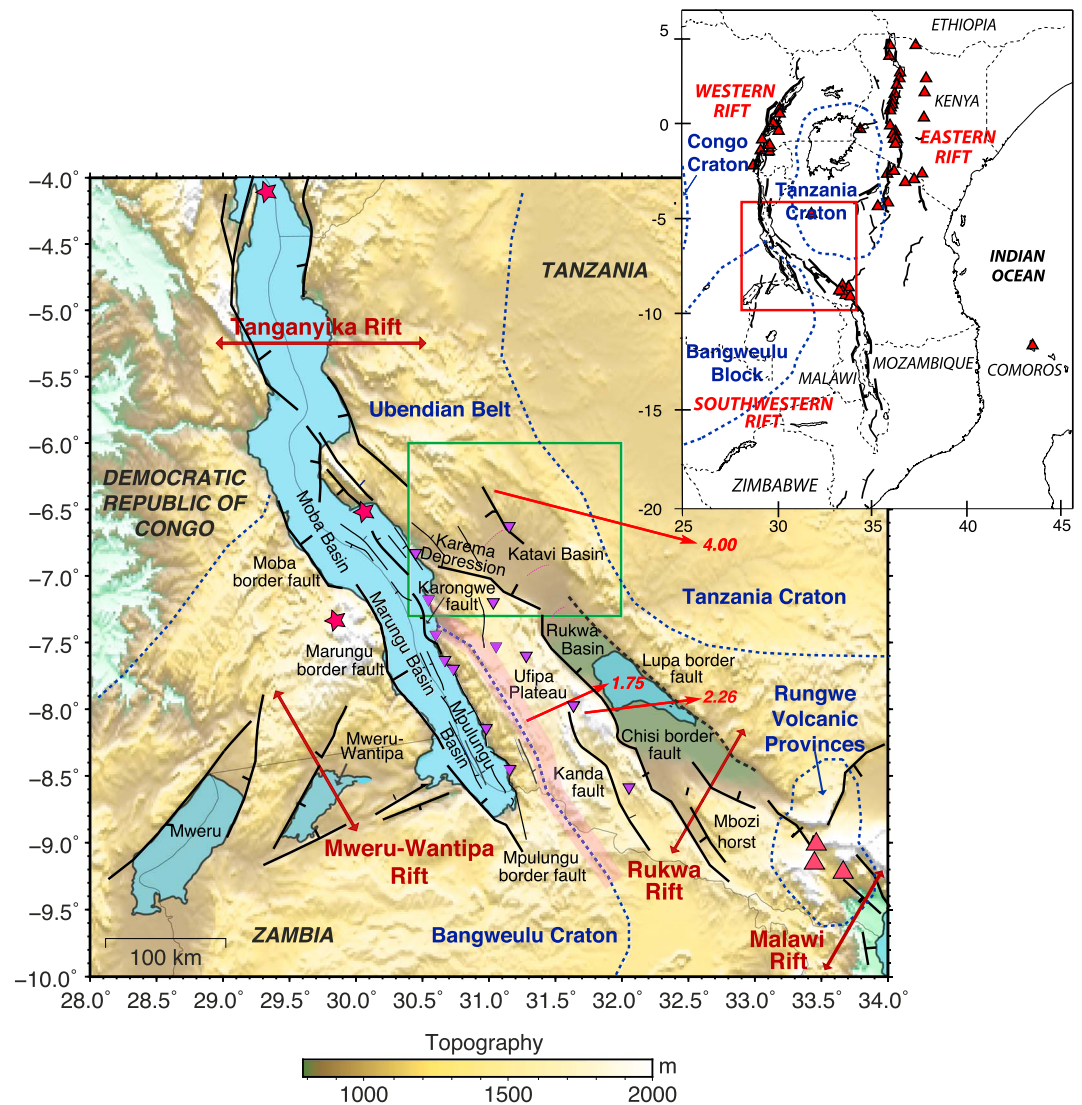


**Figure 1.** Map of the study area (after Hodgson et al., 2017; Tepp et al., 2018) with major basins, border faults, and major faults in the S. Tanganyika-Rukwa rift zone (after Delvaux et al., 2012; Ebinger, 1989; Kervyn et al., 2006; Morley, 1988). Purple inverted triangles are the array used in this study. Red arrows are extensional velocity vectors (in mm/year) from continuous GPS sites (Stamps et al., 2018). Green rectangle encloses the Katavi basin area shown in Figure 6; purple curves are beach ridges (Kervyn et al., 2006). Red stars denote hydrothermal vents (Coussement et al., 1994). Purple shaded polygon denotes the Ubendian-Bangweulu suture zone. Red triangles denote Quaternary-Holocene eruptive centers. The inset shows the S. Tanganyika-Rukwa rift zone (red box) in the context of the East African Rift.

motivated our temporary network that was designed to establish a reference for seismotectonics of the Tanganyika and Rukwa rifts.

Unlike lower crustal earthquakes and upper mantle earthquakes detected by local arrays in magmatically active sectors of the East African Rift (Keir et al., 2011; Lindensfeld & Rumpker, 2011; Weinstein et al., 2017), the deep earthquakes in the Tanganyika-Rukwa sector are the most energetic (magnitude up to 7.4) of the population (Foster & Jackson, 1998; Yang & Chen, 2010; e.g., Figure 2 and Table S1). Teleseisms with depths determined from waveform modeling show a bimodal depth distribution, leading Yang and Chen (2010) to suggest that the deeper population ( $35 \pm 5$  km) are mantle earthquakes. We use data from a 13-station temporary seismic array in the Tanganyika rift zone (Figure 1), deployed between 30 June 2014 and 1 September 2015, to determine the depth distribution of seismicity, the geometry and kinematics of border, intrabasinal and transfer faults beneath the lake basins and their uplifted flanks,

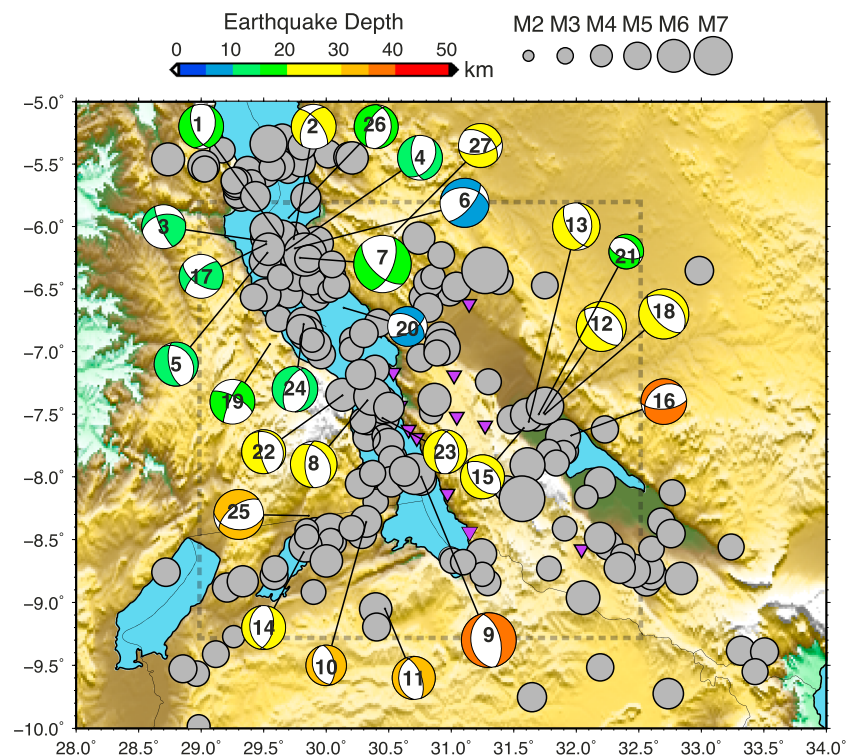


**Figure 2.** Earthquake source mechanisms and National Earthquake Information Center (NEIC) events catalog (1976–2018) within the study area. The source mechanisms exclude the Mweru rift and are as compiled by Craig et al. (2011); Ekström et al. (2012); and Yang and Chen (2010), and including mechanisms from Brazier et al. (2005); Foster and Jackson (1998); and Shudofsky (1985). Source mechanisms are scaled to local magnitude and color coded with depth; seismic catalog is scaled to local magnitude. Purple inverted triangles are the array used in this study. The focal mechanisms used are listed in Table S1. Rectangle with dashed line represents the area assumed in the Kostrov summation and stress inversion. NEIC data has been downloaded from the United States Geological Survey search website (<https://earthquake.usgs.gov/earthquakes/search/>).

allowing us to evaluate low-angle detachment and planar fault models for slip in the lower crust (e.g., Abers, 1991; Lavier & Buck, 2002). We also develop a new 1-D velocity model, a local magnitude scaling, and estimate the  $b$  value. Receiver function results from the same network (Hodgson et al., 2017) provide, for the first time, constraints on crustal thinning, allowing us to place the local and teleseismic earthquake source mechanisms within a tectonic context.

## 2. Tectonics of the Tanganyika-Rukwa Rift Zone

Active faulting and magmatism occur across a large part of the African continent from the Horn of Africa to the Comoros in the southeast and Okavango rift in the southwest (Figure 1). The broad uplifted plateaux, their corresponding negative Bouguer gravity anomalies, low upper mantle seismic velocities, and the large volume and geochemistry of eruptive volcanic products have been cited as evidence for one or more mantle plumes beneath central and eastern Africa (e.g., Ebinger & Sleep, 1998; Marty et al., 1996; Nyblade & Robinson, 1994; O'Donnell et al., 2013). Unlike the rift sectors east of the uplifted Tanzania craton, localized, relatively small melt volume of alkali, carbonatitic, and kimberlitic lavas characterize the Western rift magmatic provinces (Chakrabarti et al., 2009; Furman, 1995; Halldórsson et al., 2014).

The Tanganyika and Rukwa rifts formed in Proterozoic orogenic belts between the thick lithosphere of the Tanzania craton to the east and the Congo and Bangweulu cratons to the west and southwest (Figure 1). Fishwick and Bastow (2011) use surface wave shear velocity imaging to estimate 160- to 220-km-thick lithosphere beneath the Congo and Bangweulu cratons, relative to <150-km-thick lithosphere beneath the Western rift. Using body wave and surface wave imaging, Mulibo and Nyblade (2013), Ritsema et al. (1998),

and Weeraratne et al. (2003) determine lithospheric thickness of ~170–200 km beneath the central Tanzania craton. Although spatial gaps remain in our knowledge of the Western rift, the lowest *P* and *S* wave velocity regions underlie isolated volcanic provinces (e.g., Accardo et al., 2017; Mulibo & Nyblade, 2013; O'Donnell et al., 2013). Mantle anisotropy patterns determined from SKS-splitting measurements for the Tanganyika-Rukwa-Malawi rift region are consistent with asthenospheric flow around cratonic roots, possibly enhanced by oriented melt pockets beneath the Rungwe Volcanic Province (Tepp et al., 2018).

Our focus is the southern Tanganyika and western Rukwa rift, north of the Rungwe volcanic province (Figure 1). The NE trending Southwestern rift and the NS trending Western rift intersect in the southern Tanganyika rift. The Proterozoic lithosphere between the Bangweulu and Tanzania cratons shows a variety of regional strain fabrics and structural orientations, ranging from NNW to NW in the Tanganyika-Rukwa area, to EW along the southern boundary of the Tanzania craton (e.g., Fritz et al., 2013). Some of the study area was affected by Permo-Triassic (Karoo) rifting. The NW striking Rukwa rift contains up to 10 km of Karoo, Cretaceous, Oligocene, and Late Miocene-Recent strata (e.g., Hilbert-Wolf et al., 2016; Morley et al., 1992; Van der Beek et al., 1998). The Rukwa rift is linked to the Tanganyika rift through the Karema depression, where dextral oblique-slip motion on faults orientated N125° transfers strain from the Rukwa rift to the Tanganyika rift (Delvaux et al., 2012; Delvaux, 2001; Ebinger, 1989; Tiercelin et al., 1988). The Katavi basin is the northernmost sector of the Rukwa rift and was filled by a lake of much larger extent in the Holocene, based on the spatial distribution of beach ridges (Figure 1; Cohen et al., 1993; Kervyn et al., 2006).

There are few constraints on Western rift initiation, with estimates of ~12 Myr from projection of modern depositional rates (Cohen et al., 1993; Scholz & Lyons, 2010) and ~17 Myr from radiometric dating of volcanic sequences in the Rungwe volcanic province (Mesko et al., 2014). Uranium-lead dates of carbonatitic tuffs interbedded with syntectonic sedimentary strata in the Rukwa rift suggest initiation may have started at 25 Myr (Roberts et al., 2012) and U-Pb dating of detrital zircons in the Lake Beds unit (post-Karoo) of the Rukwa rift indicate the existence of a lake basin by 8.7 Ma (Hilbert-Wolf et al., 2017).

The South Tanganyika and Rukwa rifts include several half-graben basins bounded by large offset normal fault systems on the western side of the rift (Figure 1). The broad Moba basin has a central horst and broad shallow platform on the eastern side of the rift (Morley, 1988; Rosendahl et al., 1992). The westward tilted Marungu (or Manda) basin is bounded on the west by the Marungu border fault and by the Karongwe fault on the eastern side. The southernmost border fault, the Mpulungu border fault, is partially submerged beneath the westernmost basin where the Mweru-Wantipa rift faults cross cut Tanganyika structures (Morley, 1988; Rosendahl et al., 1992; Figure 1). In detail, structural interpretations of the intrabasinal faults differ, owing to the large line spacing between the original seismic profiles, although unpublished industry data from the eastern side of the lake provide tight constraints on fault orientation. The multiphase Rukwa basin geometry is more complex. Thermochronological and structural studies have noted that the NNW striking Chisi fault on the western side of the Rukwa rift is the active border fault system, with little morphological or seismic evidence for faulting along the NW striking Lupa border fault to the Karoo basin (Kervyn et al., 2006; Van der Beek et al., 1998). The Rukwa basin splits into two half-grabens separated by the Mbozi horst.

Receiver function results suggest that the crust thins from about 42 km on the rift flanks to 32 beneath the fault-bounded southern Tanganyika basins, or about 24% crustal extension (Hodgson et al., 2017). Delvaux and Barth (2010) invert published source mechanisms for stress orientation in subregions of East Africa and find N51° ± N3° extension direction for the southern Tanganyika rift, and N33° ± N3° in the Rukwa rift, but each region had fewer than 10 events. Geodetic constraints are very coarse and also indicate a sub-EW extension direction at ≤4 mm/year (Saria et al., 2014; Stamps et al., 2018; Figure 1).

### 3. Data

We use new, continuous, seismic data acquired from the TANGA14 network that consists of 13 broadband seismic stations installed during June 2014 (Figure 3). All stations operated between 30 June 2014 and 1 September 2015. Nine Güralp 6TD seismometers and four Güralp ESPD seismometers were used, with both instrument types recording at 50 samples per second. Data for most stations are low noise. *P* and *S* wave

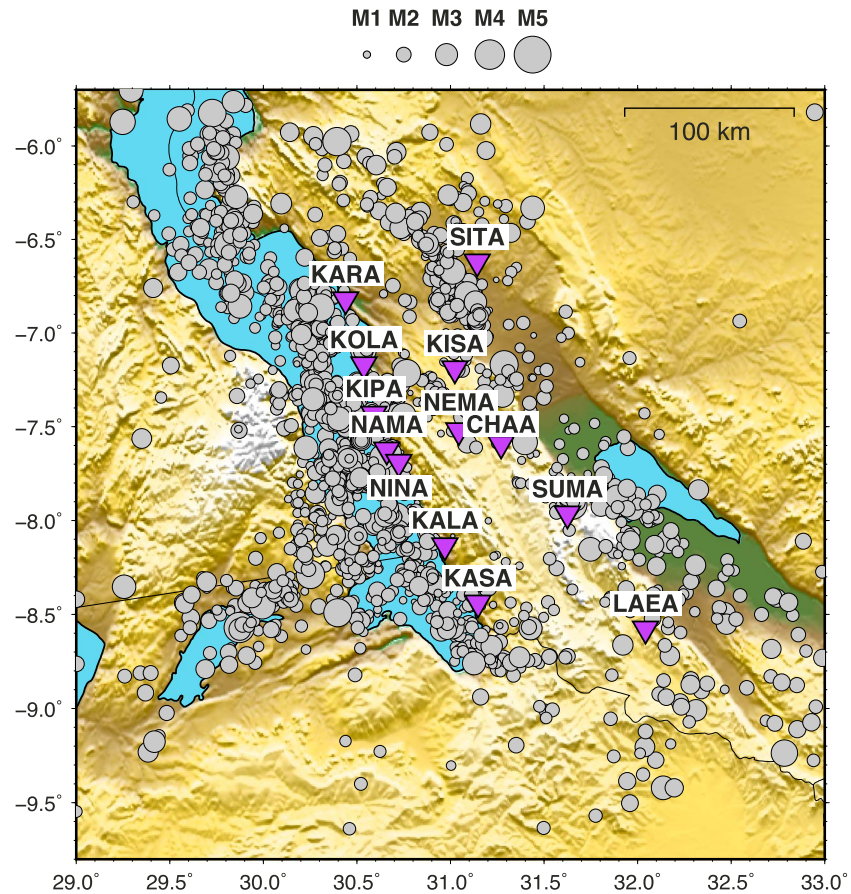


**Figure 3.** Map of the 2213 earthquakes (gray circles) scaled to local magnitude, recorded on the TANGA14 array during June 2014 to September 2015 and located using NonLinLoc (Lomax, 2008). Purple inverted triangles are the local network with station names. Earthquakes of azimuthal gap  $>200^\circ$  that are at distances from the nearest station of more than twice the earthquake depth are excluded from subsequent figures and analyses. Although outside our array, note the high level of activity in the Mweru rifts.

arrival times were picked manually for each event after applying a Butterworth band-pass filter between 2 and 15 Hz, improving the signal-to-noise ratio. Cross correlation of waveforms for an unusually deep cluster beneath the Katavi basin was used to improve  $P$  and  $S$  picks.

## 4. Methods

### 4.1. Velocity Model

Earthquake locations depend on the velocity model for the region. To obtain a suitable model, we invert the arrival time data to best fit a 1-D velocity model using the program Velest (Kissling et al., 1995). This program aims to minimize the misfit between the arrival times and the model predictions. Only events with at least six arrivals, including at least two  $S$  arrivals, and recorded with an azimuthal gap of less than  $200^\circ$  were used in the inversion. Applying these criteria results in 444 events used for the inversion of a minimum  $P$  wave velocity model (Figure 4 and Table S1). To obtain a  $V_p/V_s$  ratio representative of the selected data we compute a Wadati diagram, which yields a best fit  $V_p/V_s$  ratio of  $1.74 \pm 0.02$  (Figure S1). This value is lower than the  $V_p/V_s$  estimation of 1.75–1.97 from receiver functions (Hodgson et al., 2017) because the seismic waves from local earthquakes preferentially sample the upper crust. We started the inversion using the regional 1-D velocity model of Accardo et al. (2017; Figure 4). The raypaths rarely sample the Moho, and most of the arrivals are  $P_g$  and  $S_g$ , so we included separate constraints: an average Moho depth of 37.5 km, obtained from a receiver function analysis using the same network (Hodgson et al., 2017), and a  $P_n$  wave velocity of 8.0 km/s estimated from travel time analyses of well-located

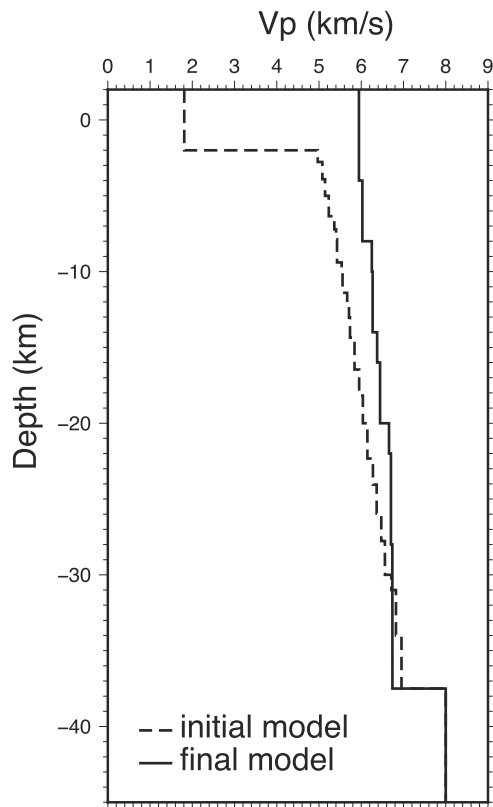


**Figure 4.** One-dimensional velocity model plot. The initial model is shown as a dashed line and the final minimum 1-D velocity model, computed using Velest (Kissling et al., 1995), as a solid line. The initial model is adapted from the Accardo et al. (2017) velocity model with Moho depth from Hodgson et al. (2017). The Pn (uppermost mantle) velocity is estimated from travel time analyses of record sections of well-located earthquakes south of the TANGA14 array, but within the combined TANGA14 and SEGMeNT arrays (Shillington et al., 2016) (Figure S2), and comparison to Pn velocities from regional tomography analyses (O'Donnell et al., 2013).

regional earthquakes (Figure S2) and from Pn tomography models that preferentially sample the rift flanks (O'Donnell et al., 2013). The inversions were stopped when the velocities did not vary significantly in the subsequent inversion. The root-mean-square error decreased from 0.828 to 0.15 s. Further tests of the stability of the model are presented in the supporting information (Figures S3a and S3b).

#### 4.2. Earthquake Location

Using the new 1-D velocity model and a  $V_p/V_s$  ratio of 1.74, we relocated 2213 events with NonLinLoc (Lomax, 2008; Figure 3 and Table S3). NonLinLoc produces an estimate of the a posteriori probability density function of the hypocenter location following the probabilistic inversion approach of Tarantola and Valette (1982) and using an oct-tree importance sampling algorithm (Lomax et al., 2000). This method allows a direct, analytical calculation of the minimum misfit origin time and hypocenter location given the observed arrival time and the calculated travel times between the stations and a point in a 3-D space. The maximum likelihood hypocenter is used in the program to calculate ray take-off angles in the first motion fault mechanism studies. From the NonLinLoc results, we select events located within the network ( $\text{gap} < 200^\circ$ ) and events outside the network are selected if the minimum distance to the closest station is less than twice the focal depth. Hence, 474 hypocentres with latitude and longitude errors  $< 1$  km and depth error  $< 2$  km are used in subsequent analyses.

#### 4.3. Cluster Relocation: Cross Correlation and HypoDD

Although several of the more intense spatial clusters of earthquakes lie at the edges or outside of our network, two clusters in the northern Rukwa rift occurred within our array (Figure 5). We relocate these two clusters using the double-difference location algorithm HypoDD (Waldhauser, 2001). Where the hypocentral separation between two events is small compared to the source-to-receiver distance and to the length scale of velocity heterogeneity, then the two raypaths between the event sources and the common station are similar (Frechet, 1985; Got et al., 1994). Therefore, we can attribute the spatial offset between

a pair of events to their difference in travel times. The residuals between observed and theoretical travel time differences are minimized for pairs of earthquakes at each station and the offset is calculated with accuracy. The lag times of cross-correlated  $P$  and  $S$  wave onsets and absolute travel time measurements are both used in the double-difference relocations. We used time windows of 3 and 4 s centered on the manual picks of  $P$  and  $S$  wave arrivals, respectively, and only used cross-correlated waveforms with a correlation coefficient greater than 0.6.

#### 4.4. Earthquake Magnitude

Seismic attenuation in the crust is an important control on the observed amplitude of phase arrivals, and hence, magnitudes. Yet attenuation varies significantly in different regions (e.g., Condori et al., 2017; Illsley-Kemp et al., 2017). Local magnitudes ( $M_L$ ) for each earthquake were estimated by first convolving the seismograms with the Wood-Anderson standard response to obtain displacement seismograms (Anderson & Wood, 1925). We then measured the maximum peak-to-peak amplitude on north-south and east-west horizontal components.  $M_L$  has been defined as (Richter, 1935)

$$M_L = \log(A) - \log(A_0) + C \quad (1)$$

where  $A$  is the observed maximum zero-to-peak amplitude of the horizontal seismogram,  $A_0$  is the empirical distance correction, and  $C$  is an empirical station correction for each component at each station. The distance correction term using a 17-km normalization (Hutton & Boore, 1987) is

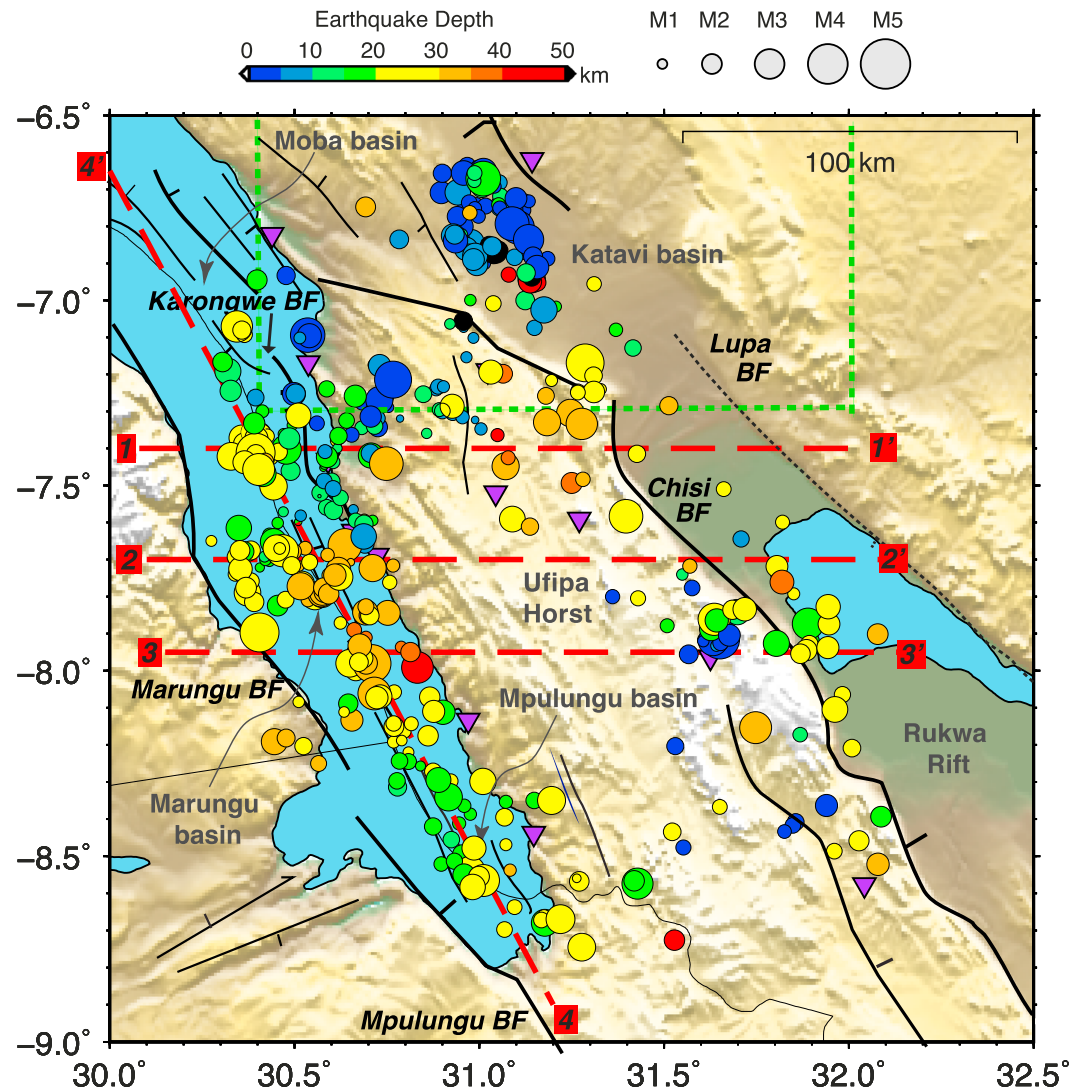


**Figure 5.** Map of epicentral locations (474 events) scaled to local magnitude and color coded with depth in a subregion of Figures 1, 2 and 3. Red dashed lines are traces of the cross sections shown in Figure 11. Main faults are highlighted in black. Purple inverted triangles denote seismometers. The green dashed rectangle encloses the Katavi basin area shown in Figure 6.

$$-\log(A_0) = n \log(r/17) - K(r-17) + 2 \quad (2)$$

where  $n$  and  $K$  are constants related to geometrical spreading and attenuation and  $r$  is the hypocentral distance of the event in kilometers. We directly solve for earthquake local magnitudes, parameters  $n$  and  $K$ , and station correction terms with a least squares criterion (Illsley-Kemp et al., 2017; Figure S2).

#### 4.5. $b$ Value

The statistical relation between earthquake frequency and magnitude provides information on expected magnitudes. In plate boundary zones worldwide, the frequency distribution of earthquakes of any given magnitude follows a log-linear relation:

$$\log N = a - bM \quad (3)$$

where  $M$  is the local earthquake magnitude and  $N$  is the number of earthquakes of magnitude larger than the magnitude threshold (Gutenberg & Richter, 1954). The largest magnitude earthquakes are rare,

**Table 1**  
Focal Mechanisms Solutions, With up to 20 Solutions and  $2\sigma$  of the Strike, Dip, and Rake (All  $\leq 35^\circ$ )

Date			Time			Longitude (deg)	Latitude (deg)	Depth (km)	Focal mechanism			# sol	$2\sigma_{\text{strike}}$	# picks	Ev #	
yyyy	mm	dd	hh	mm	ss				Strike	Dip	Rake					$M_L$
2014	07	04	00	22	45	31.0603	-6.7433	5.70	354.6	75.9	-69.3	2.2	1	5	12	1
2014	07	05	07	53	00	31.2776	-8.7450	23.08	197.0	16.0	-48.4	2.8	6	20	11	2
2014	07	05	10	05	51	31.0715	-7.4475	31.76	145.9	75.7	74.8	2.7	8	15	11	3
2014	08	01	06	24	05	30.5555	-7.7991	20.19	68.8	82.1	49.7	2.8	20	16	12	4
2014	08	11	21	14	38	30.8838	-7.2405	8.71	211.0	76.2	64.4	1.3	8	7	10	5
2014*	08	12	19	54	42	31.2702	-8.5678	23.05	141.9	85.7	-59.6	2.0	7	28	11	6
2014	09	10	01	04	56	30.7101	-7.9808	34.65	182.1	44.8	-35.5	3.8	1	5	13	7
2014*	10	10	17	30	02	30.5741	-7.7927	31.21	197.5	75.9	-68.8	2.7	15	35	9	8
2014	10	26	22	52	26	31.8687	-8.1720	14.45	317.7	75.9	69.3	1.5	1	5	9	9
2014	11	20	02	09	20	30.6242	-7.5331	11.37	158.2	75.5	-79.6	1.6	13	6	11	10
2014	01	30	22	23	23	31.1246	-6.9998	11.44	18.9	65.9	-62.8	1.9	7	7	11	11
2015	02	16	12	12	15	30.9296	-6.8251	6.68	42.3	35.5	-30.6	2.4	3	7	9	12
2015*	02	16	12	40	13	30.9356	-6.8384	3.01	34.5	36.9	-36.3	2.4	18	26	10	13
2015	02	22	01	54	50	30.7298	-7.2696	3.98	37.4	37.5	0.0	2.7	2	2	11	14
2015	02	23	07	53	31	30.3944	-7.4117	24.49	12.6	37.7	-65.0	3.9	2	5	13	15
2015	03	13	00	19	25	30.6189	-7.7268	32.77	158.6	30.4	-80.1	2.4	15	15	14	16
2015*	03	13	04	19	28	31.3976	-7.5836	27.69	19.5	77.3	35.0	3.4	7	23	13	17
2015	03	27	00	19	25	31.0108	-8.5660	28.48	320.0	55.1	3.5	3.2	1	0	13	18
2015	03	29	08	09	45	30.6224	-7.7471	28.40	225.6	45.1	-83.4	2.7	8	11	11	19
2015	04	12	07	37	59	30.3281	-7.4215	22.15	178.3	41.0	-81.3	2.8	20	20	12	20
2015	08	10	12	13	46	30.7669	-7.2135	0.10	23.5	58.2	-45.3	3.7	19	11	10	21

Note. Focal mechanisms are plotted on Figure 8. All events are included in the stress inversion and Kostrov summation (Figure 10).

whereas small magnitude earthquakes are common. The slope of the curve,  $b$ , is inversely proportional to the plate boundary stress (Scholz, 1968). We use the Maximum Likelihood method of Woessner and Wiemer (2005) in order to calculate the Gutenberg-Richter relationship with the maximum curvature estimation of the magnitude of completeness,  $M_c$ .

#### 4.6. Focal Mechanisms

None of the 474 earthquakes within the array were large enough magnitude to adequately determine source mechanisms from full moment tensor inversion. We use the first-motion modeling program FOCMEC (Snoke, 1984), which assumes a double-couple solution. The take-off angle and back azimuth from the NonLinLoc solution and polarity of the vertical waveform are used in the grid search algorithm for best fitting nodal planes, and  $P$  and  $T$  axes. Earthquakes with clear  $P$  arrivals on eight or more stations and with azimuthal gaps  $\leq 250^\circ$  were screened for focal mechanism solutions. Of the  $\sim 200$  earthquakes considered, 17 had strike, dip, and rake of the better constrained slip plane with  $2\sigma \leq 20^\circ$  and an additional 4 had  $2\sigma \leq 30^\circ$  (Table 1). Owing to the locally complex crustal velocity structure that adds uncertainty to take-off angles from event relocations, we allowed one  $P$  phase error if within  $5^\circ$  of a nodal plane.

#### 4.7. Stress Inversion and Kostrov Summation

Given the long earthquake cycle and the very short time period of our network, we compare and contrast strain rates and relative plate velocities in the S. Tanganyika rift using both local and teleseismically detected earthquakes (e.g., Weinstein et al., 2017). We take two approaches. The first is an inversion for principal stresses using the grid search algorithm of Hardebeck and Michael (2006) as modified by Martínez-Garzón et al. (2014). Uncertainties are quantified using the bootstrap method with 200 random solutions, assuming 95% confidence limits. Only one nodal plane is used in each iteration, with the preferred nodal plane being that which is optimally oriented to a given stress state, using the approach of Vavryčuk (2014). We invert both our new focal mechanisms (21 events, see section 5.4) and the catalog of moment tensors from waveform modeling (27 events; Table S1; Brazier et al., 2005; Craig et al., 2011; Ekström et al., 2012; Foster & Jackson, 1998; Shudofsky, 1985; Yang & Chen, 2010). The stress ratio



parameter,  $R$ , is also estimated. The second approach is the Kostrov summation, which provides the average of the individual moment tensor components weighted by magnitude (Kostrov, 1974). The Kostrov summation and strain rate calculation were performed over the area indicated on Figure 2, assuming a uniform seismogenic thickness of 40 km (total volume of  $\sim 6.0 \times 10^6 \text{ km}^3$ ), with a shear modulus of 30 GPa, over the 483 months (July 1977 to October 2017) of the teleseismic catalog. The comparison of the local and teleseismic stress inversions, and the Kostrov and stress inversions provides some indication of the tectonic significance of the small magnitude earthquakes, which may be influenced by local, rather than tectonic, stresses.

## 5. Results and Interpretations

### 5.1. Earthquake Locations

The 474 well-constrained absolute locations that are used in all subsequent analyses have mean relative location errors of 500 m N-S, 700 m E-W, and 900 m in depth. Earthquake activity is most intense beneath southern Lake Tanganyika, and at a specific cluster at the northern end of the Rukwa rift, beneath the Katavi basin (Figure 5). The Mweru-Wantipa rift is also seismically active, but location errors preclude further analyses of events outside our network (Figure 3). Seismicity in the Rukwa rift is localized on the western side of the rift (Chisi fault, Figure 5).

The earthquakes are distributed in discrete, 20- to 30-km-long, NS to NNW striking clusters (Figure 5). These dimensions are similar to the  $\sim 30$ -km long intrabasinal and Ufipa horst faults (Figures 1 and 5). The persistent seismic activity at the northern projection of the Chisi fault hints at active northward propagation of the Rukwa rift along the eastern flank of the Tanganyika rift.

### 5.2. Shallow Cluster in the Katavi Basin

We use the double difference method to relocate 54 shallow events (79% of the initial input) and 11 deep ( $>50$  km) events (85% of the initial input) beneath the northern Rukwa rift (Figures 5 and 6). After relocation the mean relative error decreases to 115 m N-S, 160 m E-W, and 220 m in depth for the shallow events and to 120 m N-S, 195 m E-W, and 215 m in depth for the deep events.

Most of the Katavi basin earthquakes occur at shallow depths of 0 to 15 km (Figure 6). They correlate with the NS- striking, morphologically young faults seen in the topography and in high-resolution imagery (Kervyn et al., 2006; Figure 6). These events occurred throughout the time period of the study, not in a single temporal cluster, and the rest of the region is seismically quiet. The E-W profile (B-B') through the northern group of events (Figure 6c) shows earthquakes from the surface to the middle-to-lower crust. The largest magnitude earthquake ( $M_L = 3.5$ ) along this profile is the deepest event at  $\sim 20$  km. Some of the earthquakes occurred beneath steep NS faults that displace Holocene sediments and former lake strand lines (Ebinger, 1989; Kervyn et al., 2006; Figure 6).

### 5.3. Magnitudes and $b$ Value

For the Tanganyika rift, we find that the geometrical spreading constant  $n$  is 0.736 and the attenuation constant  $K$  is  $2.24 \times 10^{-3}$ . Equation (2) becomes

$$-\log(A_0) = 0.736 \log(r/17) - 2.24 \times 10^{-3} (r-17) + 2 \quad (4)$$

where  $r$  is the distance in kilometers. The local magnitude ( $M_L$ ) of earthquakes in the study area varies between 0 and 4.69, with an average of 1.67. The local magnitudes of the well-located 474 events range from 0.35 to 3.98 with an average of 1.85.

We use the complete catalog of 2213 events with magnitude determinations  $0 \leq M_L \leq 4.69$  in order to derive a Gutenberg-Richter relation of  $\log N = 4.22 - 0.75 M$ . The maximum curvature method, including the correction factor of 0.2, yields  $M_c = 1.9$  (Woessner & Wiemer, 2005; Figure 7). Bootstrap uncertainties of the  $a$  and  $b$  values are  $\pm 0.05$  and  $\pm 0.02$ , respectively. We find that the  $M_c$  agrees well with studies using similar station spacing (i.e., Illsley-Kemp et al., 2017). Our catalog spans a total of 14 months, leading to an undersampling of larger magnitude events. Our  $b$  value estimate of  $0.75 \pm 0.02$  (Figure 7) is less than the  $b$  value of 0.84 for Tanzania, which includes the Archaean craton (Langston et al., 1998), and that of magmatic rift sectors:

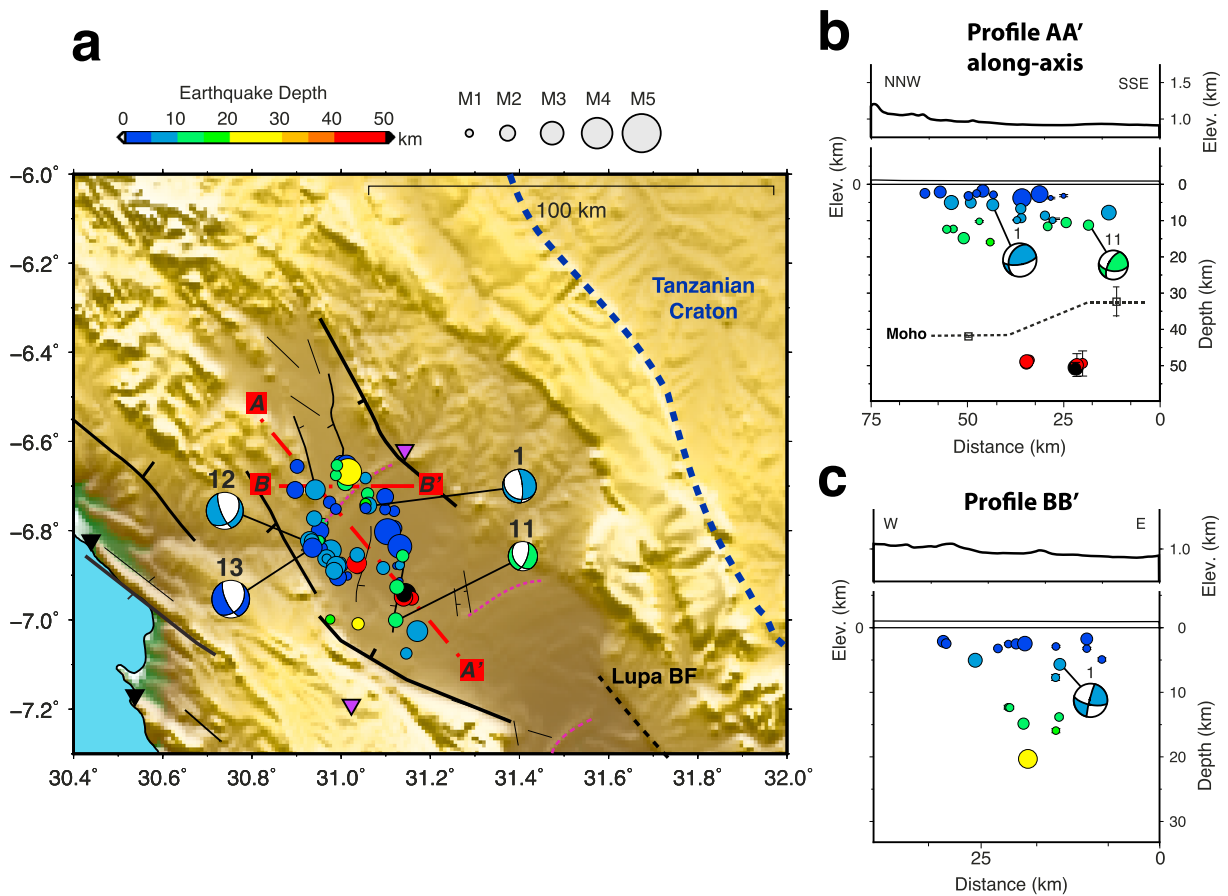


**Figure 6.** (a) Map of double-difference earthquake relocations of the Katavi basin cluster at the northern end of the Rukwa rift. The red dashed lines are the traces of the cross sections shown in (b) and (c). Main faults are highlighted in black (Ebinger, 1989; Kervyn et al., 2006), and the dashed line is the Permo-Triassic Lupa border fault. The purple dashed lines represent ancient lake shorelines (Kervyn et al., 2006). The blue thick dashed line is the limit of the Tanzania Craton. (b) Along-axis profile AA' striking NNW-SSE. (c) Across-axis profile BB'.

$0.87 \pm 0.03$  estimated for the Magadi-Natron-Manyara rift zone (Weinstein et al., 2017) and  $0.87$  for the central Kenya rift (Tongue et al., 1994).

#### 5.4. Earthquake Source Mechanisms

First-motion focal mechanism solutions for earthquakes in the crust show a full range from normal dip slip to strike slip, and even reverse faulting for small magnitude events. Many of the earthquakes with dip-slip mechanisms have steep nodal planes ( $\geq 45^\circ$ ) even at depths of 30–35 km (e.g., events 7 and 16; Table 1 and Figure 8). As in earlier studies of teleseismic events (e.g., Craig et al., 2011; Yang & Chen, 2010), several mechanisms have one near-vertical plane (e.g., events 1, 2, 5, 6, and 8; Table 1 and Figure 8). The low-angle nodal planes of these events, however, are oriented highly oblique to the mapped faults and regional extension direction and are less likely.

#### 5.5. Earthquake Depth Distribution

The depth distribution of earthquakes relocated using the new minimum 1-D velocity model and NonLinLoc shows that most of the fault rupture initiates in the middle-to-lower crust beneath the Tanganyika and Rukwa rifts (Figure 9). Exceptions are the shallow events beneath the Rukwa rift that are mainly localized beneath the Katavi basin (Figures 5 and 6). The database shows that earthquakes are distributed throughout the crust (32 to 42 km), with a gap between 42 and 48 km, and the upper mantle events (48–52 km) are mostly localized beneath the Katavi basin (Figures 5, 6, and 9). Patterns in the Tanganyika and Rukwa basins reveal continuous seismicity from surface to  $\sim 40$  km (Figure 9).

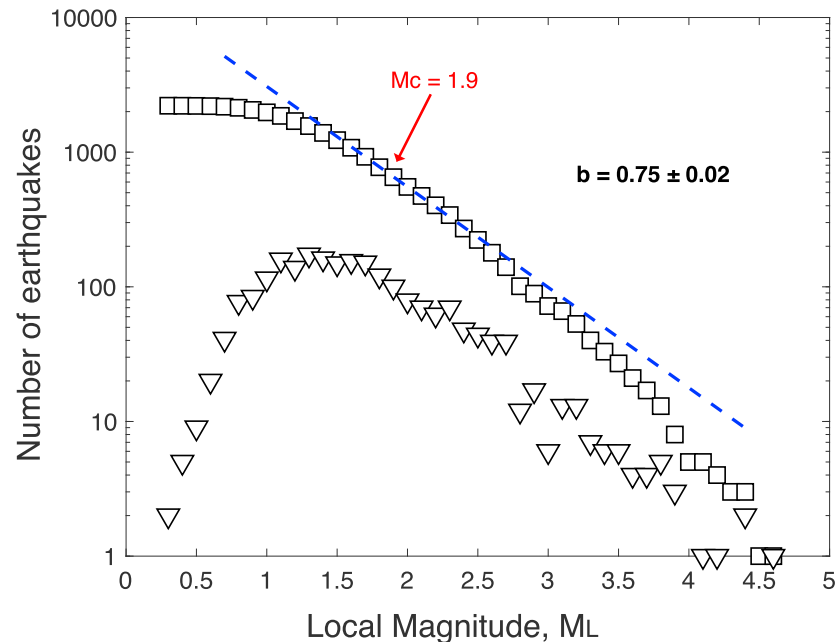


**Figure 7.** Using the local magnitude scaling and the adjusted maximum curvature method of Woessner and Wiemer (2005), we determine a magnitude of completeness ( $M_c$ ) of 1.9. Using the entire magnitude range method of Woessner and Wiemer (2005) results in a  $b$  value of  $0.75 \pm 0.02$  for the dataset with the full catalog of 2,213 locations.

### 5.6. Rift Kinematics

Given the relatively small number of earthquake focal mechanisms in the local ( $N = 21$ , Table 1) and teleseismically detected ( $N = 27$ ; Table S1) catalogues, we did not separate the Tanganyika and Rukwa areas for full analysis, as was done in the earlier study of Delvaux and Barth (2010).

#### 5.6.1. Local earthquakes

The local earthquake inversion shows a NE-SW extension direction ( $\sigma_3 = N240^\circ$ ) with  $<10^\circ$  plunge, and  $R = 0.41$  (Figure 10a). The uncertainty in  $\sigma_3$ , or  $T$  axis direction, is  $+25^\circ/-15^\circ$ . The Kostrov summation results show a  $T$  axis at  $N255^\circ$ , but with a smaller plunge and near vertical  $\sigma_1$  or  $P$  axis (Figure 10b).

#### 5.6.2. Teleseismically detected earthquakes

The compilation of earthquake depths determined from waveform modeling from Craig et al. (2011) and Yang and Chen (2010) forms the basis for similar analyses (Figure 2 and Table S1). Note that the location errors of these earthquakes may be 30 km or more. The  $\sigma_3$  direction is  $80^\circ \pm 15^\circ$  and  $R = 0.51$  (Figure 10c). The Kostrov summation for the 40-year teleseismic record within our study area provides a  $T$  axis ( $\sigma_3$ ) of  $N80^\circ E$  and an extensional strain rate of  $7 \times 10^{-17}/s$  or  $2 \times 10^{-9}/year$  (Figure 10d). The seismically determined extension direction is the mean of the opening directions from two GPS measurements ( $N76^\circ-83^\circ$ ). The seismic strain rate is about five times smaller than the average geodetic strain rate in the same area (Stamps et al., 2018). The discrepancy between seismic and geodetic strain estimates is small compared to magmatic rifts where the discrepancy is more than 30%, owing to aseismic strain accommodation by magmatic processes (e.g., Weinstein et al., 2017).

The Kostrov and stress inversion results for the teleseisms (Figures 10c and 10d) are nearly identical and are very similar to the local earthquake extension direction estimates (Figures 10a and 10b). The similarity between all results indicates that the microseisms generally provide information on tectonic processes, although the larger scatter in the local stress inversion suggests that local processes may contribute to fault kinematics. With this information on regional stress as well as the strike and dip of faults throughout the region, the  $<20^\circ$  nodal planes of our events 1, 5, 9, and 10 are oriented unfavorably to the stress, and the steep plane is the more likely slip plane (Figures 8 and 10).

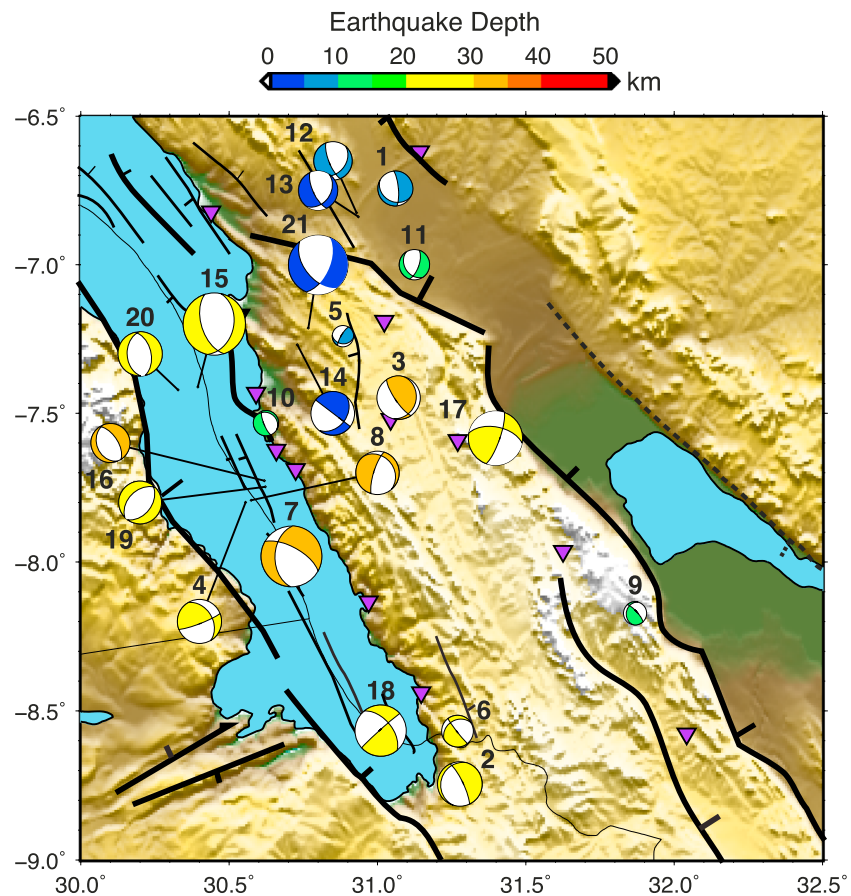


**Figure 8.** First motion focal mechanism solutions scaled to local magnitude and color coded with depth. Numbers next to the event refer to the event identification in Table 1. The focal mechanisms are projected in Figure 11 along the line of cross-sections shown in Figure 5.

### 5.7. Basin Profiles

We use rift perpendicular and rift parallel profiles to illustrate the 3-D structure of the basin and the geometry of border faults at depth within the crust, with particular focus on fault slip kinematics in the lower crust (Figures 5 and 11). The cross sections across the Tanganyika rift are made E-W, approximately parallel to the regional extension direction as determined from our analyses of local and teleseismic earthquakes (section 5.6 and Figure 10) and comparison with models of GPS and teleseismic data (Stamps et al., 2018; Figure 1). For the purposes of the cross sections, the dip of the border faults is assumed to be planar and  $50^{\circ}$ – $60^{\circ}$ . Intrabasinal faults are assumed to extend to lesser depths and to be steeper at  $60^{\circ}$ , based on seismic imaging and balanced cross sections (Morley, 1988). For the along-axis transect (Profile 4–4'; Figure 11a), transfer fault zones between basin segments are from Morley (1988). Faults on the Ufipa plateau are from Delvaux et al. (2012).

Profile 1–1' crosses the North Marungu basin where the basin geometry is a westward tilted full graben (Morley, 1988; Rosendahl et al., 1992; Figures 1 and 11a). The Karongwe border fault on the eastern side is about half the length of the Marungu border fault (Figure 1). Seismicity data indicate that both border fault systems are active (Figures 3 and 11a). On Profile 1–1', earthquakes with steep ( $>40^{\circ}$ ) nodal planes occur at lower crustal depths (Figure 11a). A second zone of 0- to 20-km-deep earthquakes occurs along the eastern side of the basin within the Bangweulu craton-Ubendian orogenic belt suture zone where little detailed mapping has been done (Figures 1 and 11a). Projections of the Karongwe and the Marungu border faults to depth indicate that  $\sim 25$  km is their intersection depth (Figure 11a). Either west or east dipping nodal planes could be the slip plane but either argues against a low-angle detachment beneath this basin. Regardless, the deep earthquakes have steep normal nodal planes (Figure 11a). The deepest earthquakes are at depths  $\sim 42$  km, at

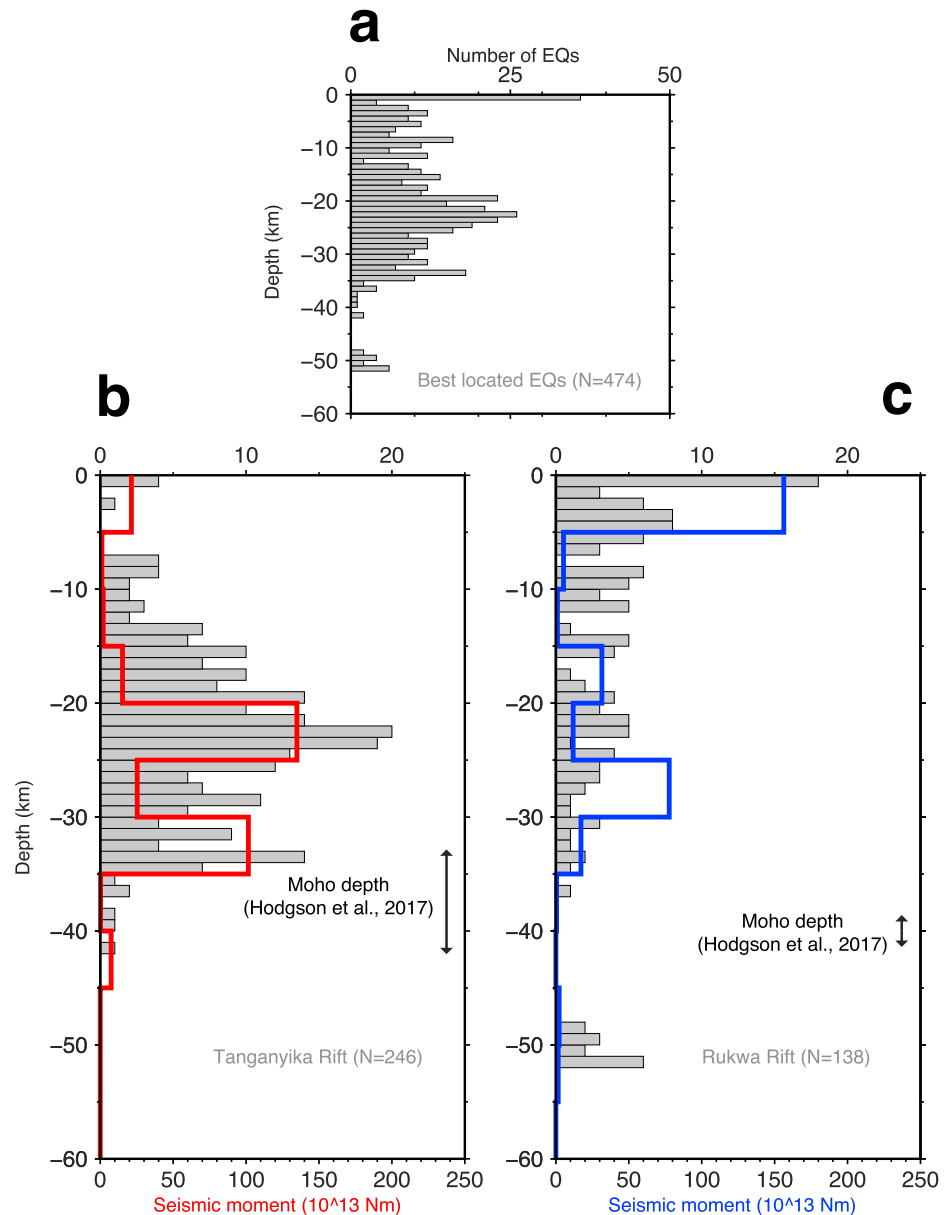


**Figure 9.** Histograms of well-constrained earthquake hypocenters (474) with 1-km depth intervals. (a) All events. (b and c) The bottom graphs separate the two regions of interest: (b) events beneath the Tanganyika rift; (c) events beneath the Rukwa rift. The red and blue lines are, respectively, Tanganyika and Rukwa seismic moment by depth with 5-km depth intervals. The seismic moment  $M_0$  (in Nm) is related to the local magnitude  $M_L$  as in Kanamori (1977, 1983):  $\log M_0 = 1.5 \times (M_L + 6.06)$ .

the crust-mantle boundary as determined from sparse receiver function data (Hodgson et al., 2017). Diffuse deep seismicity occurs beneath the uplifted Ufipa horst between the Tanganyika and Rukwa basins (Figure 11a).

Profile 2–2' (Figure 11b) and profile 3–3' (Figure 11c) cross the Central and South Marungu basins, respectively, which are westward tilted half-grabens, as is the Cenozoic Rukwa basin (Figures 1, 11b, and 11c). Receiver function data suggest that the crust thins over a short distance to less than 32 km beneath the fault-bounded basin (Hodgson et al., 2017). Projections of both the Marungu and Chisi border faults coincide with lower crustal earthquakes. The down-to-east nodal plane of earthquake 7 (Figures 11b and 11c and Table 1) matches the inferred Marungu border fault dip. Unless there is no crustal thinning beneath the

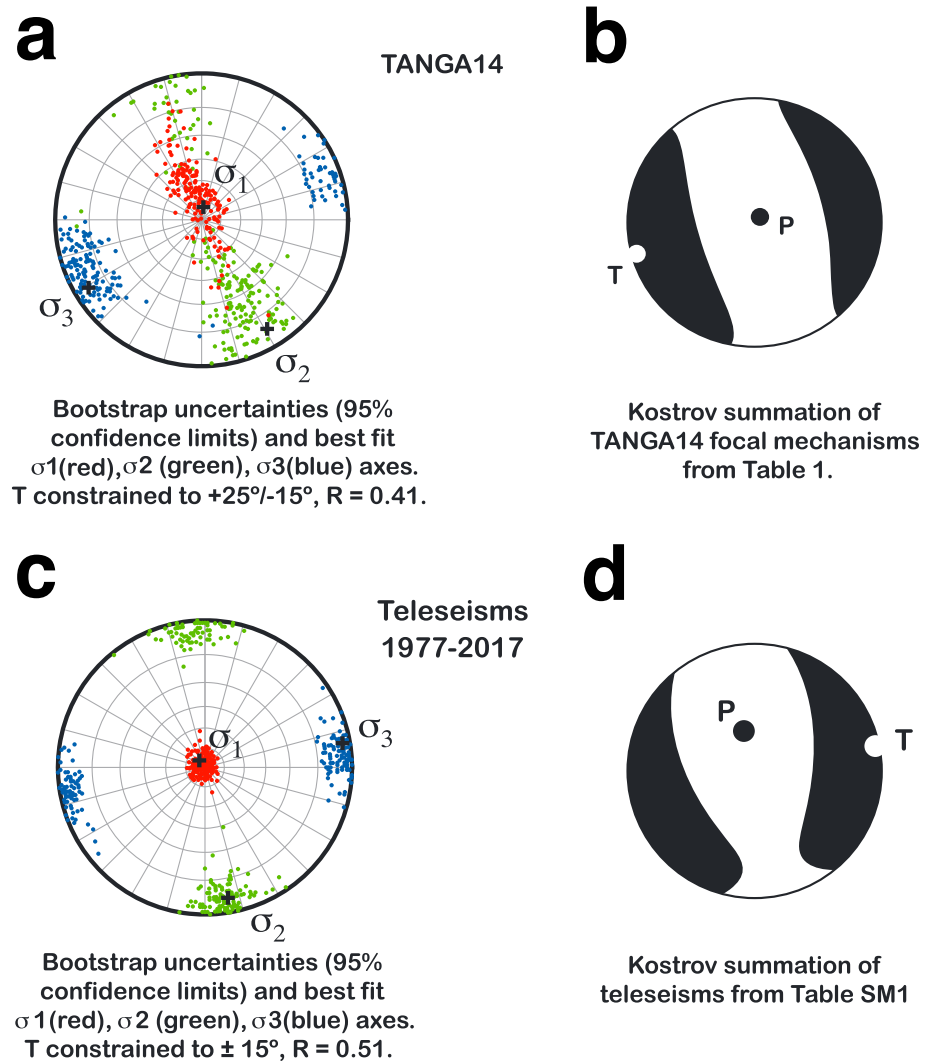


**Figure 10.** Comparison of gridsearch stress inversion using the MSATSI program (Martínez-Garzón et al., 2014) and Kostrov summation results for local (a, b) and teleseismic earthquakes (c, d) where inputs are weighted by magnitude. (a) Bootstrap uncertainties with 95% confidence limits about best fitting  $\sigma_1$ ,  $\sigma_2$ , and  $\sigma_3$  indicated by crosses, using the focal mechanisms in Table 1. (b) Kostrov summation of earthquakes in Table 1. (c) Bootstrap uncertainties with 95% confidence limits about best fitting  $\sigma_1$ ,  $\sigma_2$ ,  $\sigma_3$  indicated by crosses, using the focal mechanisms in Table 1, from the compilations in Yang and Chen (2010) and Craig et al. (2011; Table S1). Where events are duplicated in the two publications, the Yang and Chen (2010) solution was used. (d) Kostrov summation of earthquakes in Table S1. Both results indicate an approximately N80°E rift extension direction, and indicate that the largest local events are representative of tectonic stress.

7-km-deep Marungu basin, the deepest earthquakes (38–42 km) are in the uppermost mantle (Figures 11b and 11c). Along the eastern side of the profile, the Kanda and Chisi faults are seismically active with lower crustal earthquakes at depths of 35–40 km (Figures 11b and 11c).

Profile 4–4' (Figure 11d) is an along-strike profile transecting the southern Tanganyika rift from the NW to SE, from the Marungu basin in the north to the Mpulungu basin at the southern tip of the rift. The profile reveals significant along-axis variations in the depth distribution of earthquakes that correlate with along-axis segmentation (Figure 11d). The northernmost part of the profile transects the shallow platform on the eastern side of the Tanganyika rift at the Moba basin and then passes through the Marungu basin bounded by large offset, deep faults on both sides of the basin (Marungu and Karongwe border faults) and through the Mpulungu basin. Viewed in this perspective, the deepest earthquakes occur beneath the S. Marungu half-graben, which has the thickest sedimentary sequence. The transition between the two

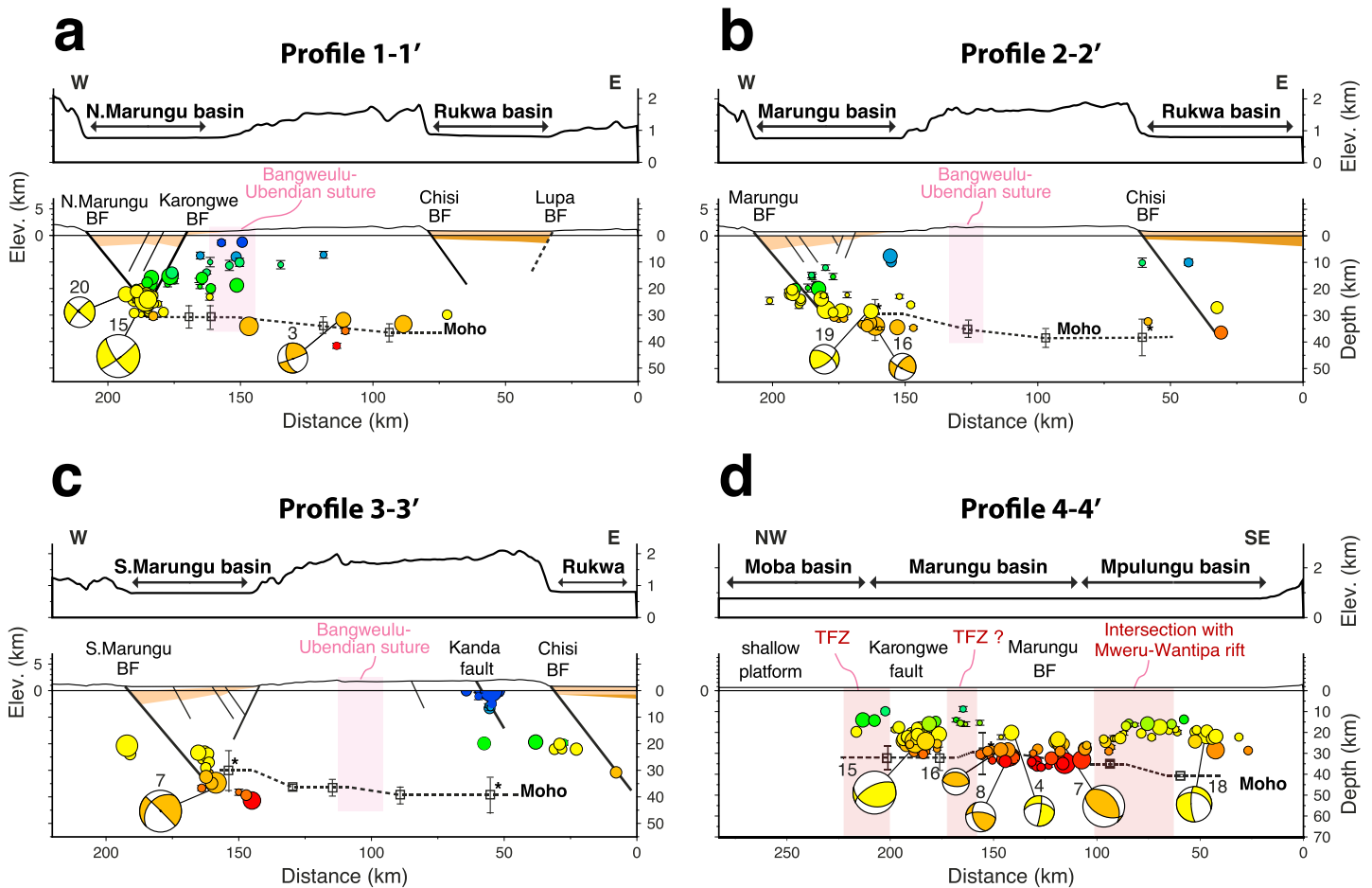


**Figure 11.** (a–c) Cross-rift profiles 1–1′, 2–2′, and 3–3′ and (d) along-axis profile 4–4′ as indicated in Figure 5. The light purple shading represents the Ubendian-Bangweulu suture zone, and the light red shading represents transfer zones as mapped by Morley (1988). Black squares mark stations with Moho depth results with their associated error bar from receiver functions (Hodgson et al., 2017). Squares with asterisk (\*) are receiver functions results with crustal thickness errors >10 km and should be treated as approximate. Note the different Y axis on profile 4–4′.

basins is a faulted ramp (transfer fault zone; Morley, 1988). Earthquake depths become shallower where the NE striking faults of the Mweru-Wantipa rift cross cut the approximately NS striking Tanganyika rift faults. The westward-tilted Mpulungu half-graben is the shallowest Tanganyika basin, and it contains a  $\leq 2$  km-thick sedimentary sequence, suggesting that it is younger than the rift basins to the north (e.g., Cohen et al., 1993). South of the Mweru-Wantipa intersection, earthquake depths increase beneath the southernmost Mpulungu basin, with events located at 20–30 km. These along-strike patterns suggest that strain decreases locally as it is transferred across a broader region.

The along-strike variations suggest that seismogenic thickness varies between basins and that full graben basins may have shallower seismogenic depths owing to the interactions between the conjugate faults at depth. Border faults bounding half-grabens appear to have deeper seismogenic depths, and they may penetrate the entire crust. Teleseismic earthquakes show similar steep nodal planes, but comparatively large location errors prevent direct correlation with specific border faults (Figure 2).

## 6. Discussion

This study and the network used have some inherent limitations for the interpretation of rifting processes and crustal rheology. We are looking at a snapshot in time of a year and a half compared to seismic cycles of tens to hundreds of years (e.g., Barbot et al., 2012; Bufe & Varnes, 1993; Dieterich, 1994). Moreover, our seismic network geometry is limited due to the poor access of the west side of Lake Tanganyika. However,

our study used well-constrained events with events outside the array ( $200^\circ < \text{azimuthal gap} < 260^\circ$ ) selected only if their epicentral distance to the closest station is less than twice the focal depth. All selected events have errors in locations and depth of less than 1 km. We also consistently used events located near or inside the array (azimuthal gap  $\leq 250^\circ$ ) to determine focal mechanisms. The close similarity of source mechanisms of local earthquakes with  $1.9 < M_L < 3.98$  and teleseismically detected earthquakes from a much longer time period indicate that the local earthquakes are primarily caused by tectonic stresses.

The new constraints on the depth of the Moho (Hodgson et al., 2017) allow us to evaluate the geometry, kinematics, and depth extent of border faults, to reconsider depth distributions, interpreted from limited teleseismic earthquakes, and to place the persistent, and sometimes large magnitude ( $M_w > 6$ ), lower crustal earthquakes, typical of the Western rift of the EARS, in tectonic context.

### 6.1. Distribution of Active Faulting

One clear result of our study is the documentation of an approximately 350-km-wide zone of seismically active faults at the junction of the Mweru-Wantipa, Tanganyika, and Rukwa rifts, where damaging earthquakes have occurred in the past (e.g., Ambraseys & Adams, 1992). It is important to note that the northern part of the uplifted Ufipa plateau as well as the Kanda fault are seismically active, indicating that some uplifted flanks are actively deforming (Figures 5 and 11).

Without direct observations of the Moho depth beneath the faulted rift basins, we can only assume that the crust beneath the central basins is the same or less than beneath the eastern side of the basins: approximately 32 km (Hodgson et al., 2017), as shown in our cross sections (Figure 11). Our study shows continuous seismicity throughout the crust with unusually deep events localized at Moho depth beneath the S. Marungu basin. The apparent seismic gap between 40- and 48-km depth in the Rukwa basin corresponds to the crust-mantle boundary beneath the northern Rukwa rift, based on receiver function results from this network (Hodgson et al., 2017; Figures 6 and 9). The earthquakes at 48- to 52-km depth beneath the Katavi basin (Figure 6b), therefore, occurred in the upper mantle, and they are the topic of further analyses.

Earthquakes in the separate and combined Rukwa and Tanganyika sectors (Figure 9) show a continuous depth distribution over the range of measured crustal thickness, arguing against a bimodal depth distribution implied by a small number of teleseisms (15–20 km, 30–40 km) in Yang and Chen (2010). The two peaks in energy for the Tanganyika rift (20–25 and 30–35 km; Figure 9b) are related to the N. Marungu basin earthquakes (peak at 20–25 km) and to the S. Marungu basin earthquakes (peak at 30–35 km), respectively. Although they may be an artifact of the short time period of observation, they could be linked to along-axis segmentation. The 25- to 30-km peak in Rukwa earthquake depth distribution (Figure 9c) is likely due to a larger event in the middle-to-lower crust, making it a likely artifact of our short period of observations. Regardless, this result, combined with the depth distribution of lower crustal earthquakes, suggests a strong lower crust in an area of thinned lithosphere. The zones of lower crustal earthquakes are not restricted to cratonic lithosphere; they occur in both the Bangweulu craton (Marungu, Mpulungu border faults) and the Ubendian belt (Chisi border fault; Figure 5). Earthquake source mechanisms provide additional constraints, as outlined below.

### 6.2. Steep and Deep Border Faults

Balanced cross sections of seismic data indicate that most of the extension across Tanganyika half-graben and full-graben basins is achieved by slip along the border faults (Figure 11; Morley, 1988). Our results show that steep, seismically active, planar border faults penetrate the entire crust at present. Stratal and fault geometry indicate that the border faults have been the locus of strain since early in the basin history (Muirhead et al., 2019) and thermomechanical models of the topography and gravity anomalies across the Tanganyika rift are consistent with steep, deep border faults (Ebinger et al., 1991). They form in strong lithosphere and explain the broad, deep basins and broad high flanks (e.g., Ebinger et al., 1991; Ellis & King, 1991). These earlier studies focus on time-averaged deformation, whereas our active deformation study provides only a snapshot of longer-term isostatic compensation processes.

The seismicity in some parts of the rift illuminates steep and sometimes very deep faults, with the deepest earthquakes correlating with projections of the border faults to lower crustal depths (Figure 11). Some of the normal fault earthquakes at depths of 20–40 km have two steep nodal planes (events 15, 19, and 20;



Table 1 and Figures 8 and 11). For the other deep earthquakes at 20- to 40-km depth, the preferred nodal plane based on orientation with respect to  $\sigma_3$  (extension) is the steeper nodal plane (events 2 and 6; Table 1 and Figure 8). The parallelism of nodal planes of focal mechanisms with projections of border faults to lower crustal levels indicates that the deep earthquakes beneath the Marungu and Mpulungu basins correlate with slip along the border faults (e.g., Figure 11). These patterns are consistent with the time-averaged deformation patterns (Morley, 1988; Muirhead et al., 2019). The along-strike and cross-rift profiles and earthquake nodal planes argue against the presence of a low-angle detachment fault (Figure 11), as is found in some collapsing orogenic belts (e.g., Abers, 1991; Axen, 1992).

Camelbeeck & Iranga (1996) made a similar interpretation of lower crustal faulting along steep, deep border faults in cold, strong lithosphere from seismicity data in the southern Rukwa rift. Similar patterns are seen in the Rwenzori sector of the Western rift (Lindenfeld et al., 2012), and the Natron and Manyara basins of the Eastern rift (Albaric et al., 2013; Weinstein et al., 2017). The intrabasinal faults and faults on the Ufipa plateau between the Tanganyika and Rukwa rifts have two nodal planes with dips  $\geq 45^\circ$  (events 11, 13, and 21, Table 1, Figure 8).

### 6.3. Extension Direction and Influence of the Ubendian-Bangweulu Suture Zone

The stress inversion and Kostrov summation analyses of local and teleseismic earthquakes indicate an extension direction of about N80°E, consistent with the range of opening directions (76°–83°N) from GPS data along the Ufipa plateau (Stamps et al., 2018; Figures 1 and 10). Earlier studies of much smaller datasets suggested a NE extension direction (Brazier et al., 2005; Delvaux et al., 2012). Brazier et al. (2005) noted a mix of left and right lateral strike-slip motion along ENE and NE striking nodal planes and interpreted a complex stress regime. Sinistral and dextral motions are expected in a finite width plate boundary zone where 80- to 120-km-long border faults are linked by relay ramps and oblique-slip faults that interact in space and time (Ebinger, 1989; Morley, 1988).

The Bangweulu craton-Ubendian belt suture zone may also influence fault geometry and kinematics. Indeed, many of the earthquakes show oblique-slip or strike-slip motion, particularly east of the Katavi basin where the Bangweulu-Ubendian suture zone curves to NW (Boniface & Appel, 2018) and where NE and EW striking faults of the Mweru-Wantipa rift intersect the Tanganyika rift faults (Figures 1 and 11). It is possible, therefore, that the strike-slip and oblique-slip mechanisms involve slip along preexisting basement structures.

### 6.4. Along-Axis Variations

Comparisons of seismogenic layer thickness, orientation and dips of faults from focal mechanisms, and basin architecture show significant along-axis differences between the Marungu and Mpulungu basins. Along the length of the N. Marungu basin, the seismicity is localized at the intersection of the conjugate N. Marungu and Karongwe border faults where the basin approaches a full-graben form (Figure 11a). Seismogenic layer thickness is shallower (~25 km) in the N. Marungu basin than the westward-tilted S. Marungu half-graben to the south (~40 km; Figure 11d). The along-strike variations in seismogenic layer thickness suggest that discrete border faults penetrate to different crustal levels. Although the number of basins studied is small, we see deeper earthquakes in the half-graben basin than the full-graben basin. Without constraints on crustal stretching, we cannot determine whether more stretching has occurred across the N. Marungu (full-graben) sector than the S. Marungu sector (half-graben) or if stress interactions between conjugate faults plays a role. Mweru-Wantipa faults intersections of the Mpulungu basin may also explain the smaller seismogenic layer thickness between 65 and 100 km along profile 4–4' (Figure 11d), which then increases to the southern, half-graben sector of the basin (60 km, Figure 11d).

Assuming an average slip of 1 m, a shear strength of 32 GPa, a seismogenic layer thickness of 25 to 50 km, a fault rupture length of 30 km, and a dip of 60°, we estimate a potential earthquake of Mw 6.9 to 7.1 along Tanganyika border faults. These magnitude estimates surpass the Mw 6.5 earthquake of October 2000 beneath the Mpulungu basin and the Mw 6.8 beneath the Marungu basin in December 2005 (Table S1). If the entire Marungu border fault (~110-km-long) were to rupture a 40-km seismogenic layer, empirical relations suggest at least 3 m of slip along the fault (Wesnousky, 2008). A similar estimate of magnitude, using previously mentioned parameters, would result in a Mw 7.7 earthquake, which surpasses the largest recorded African earthquake: the 1910, Ms 7.4, Rukwa earthquake (Ambraseys, 1991). The historic

seismicity (e.g., Figure 2) and our estimates suggest that less than 30-km-long ruptures are more typical of Tanganyika and Rukwa rifts activity, but that an entire border fault rupture is possible.

### 6.5. Implications for Lower Crustal Deformation Processes

Previous studies indicate that the crust and mantle lithosphere beneath the southern Tanganyika and Rukwa rift zones have experienced relatively minor thinning of cold, strong cratonic lithosphere over the past ~15 Myr (e.g., Accardo et al., 2017; Fishwick & Bastow, 2011; Hodgson et al., 2017). Assuming a low geothermal gradient and extrapolating laboratory measurements to very slow tectonic strain rates, dry granulite or mafic lower crust could retain strength at 35- to 40-km depth, leading Craig et al. (2011), Foster and Jackson (1998), Mulibo and Nyblade (2013), Shudofsky (1985), and Yang and Chen (2010) to interpret dry, mafic lower crust as the explanation for lower crustal earthquakes. Alternatively, some of the earthquakes may occur in a strong upper mantle (Déverchère et al., 2001; Yang & Chen, 2010), or in response to rapid stressing of more ductile material by magma intrusion (e.g., Albaric et al., 2013; Weinstein et al., 2017). The  $V_p/V_s$  ratio from receiver function studies indicates that both the Ubendian belt and Bangweulu craton crust have a felsic bulk composition (Borrego et al., 2018; Hodgson et al., 2017; Tugume et al., 2012). Elevated  $V_p/V_s$  values ( $\geq 1.9$ ) are determined within the fault-bounded Marungu and Mpulungu basins, which have hydrothermal vent sites and hot springs along the margins, leading Hodgson et al. (2017) to suggest that magma intrusion may be occurring beneath the southern Tanganyika rift. The upper mantle earthquakes beneath the Katavi basin on the eastern flank of the Tanganyika rift (Figure 6) may be associated with volatile release from metasomatic reactions or magma intrusion, as inferred for the Rwenzori rift sector (e.g., Lindenfeld et al., 2012).

Our preferred interpretation of the deep earthquakes beneath the southern Tanganyika and northern Rukwa rifts is that the intrabasinal and Ufipa plateau faults penetrate to ~15 km, whereas the border faults penetrate the entire crust, which may vary in thickness along the length of the rift (e.g., Figure 11). The border faults initiated and grew to become the largest faults during the earliest stage of rifting, possibly enhanced by volatile release from initial impingement of a mantle plume that metasomatized the mantle lithosphere (e.g., Ebinger et al., 2017; Roberts et al., 2012). After 12 Myr or more, the border faults continue to accommodate the majority of brittle strain across the basins.

## 7. Conclusions

The 13-station TANGA14 temporary array recorded 2213 earthquakes of magnitude  $0 < M_L < 4.69$ , with a magnitude of completeness of 1.9 and  $b$  value of  $0.75 \pm 0.02$ . Using a new local velocity model, we relocate 474 earthquakes in the southern Tanganyika and northern Rukwa rifts. They occur from 0 to 52 km below sea level, with no gap in seismicity between 0 and 42 km, which is the maximum crustal thickness in the region determined from receiver function analyses (Hodgson et al., 2017). Using a new local magnitude scaling that accounts for local attenuation, the magnitudes of the 474 earthquakes with well determined locations are  $0.35 < M_L < 3.98$ . The lower crustal earthquakes beneath the Tanganyika rift are some of the largest magnitude earthquakes in the database.

Earthquake deformation occurs across an approximately 350-km-wide zone from the Mweru-Wantipa rift (Southwestern rift system) to the Rukwa rift. Stress inversion and Kostrov summation of the source mechanisms of 21 local and 27 teleseismically detected earthquakes from the south Tanganyika and north Rukwa rifts are in good agreement and they indicate a  $N80^\circ$  extension direction that is parallel to the opening direction from geodetic data (Stamps et al., 2018).

Border faults and intrabasinal faults are seismically active in the Tanganyika and Rukwa rift, as well as faults on the Ufipa horst. Segments of the suture zone between the Ubendian orogenic belt and the Bangweulu craton are also seismically active. Border faults, which have accommodated the majority of the extension across half-graben basins over the past ~12 Myr, are associated with earthquakes occurring from the base of sediments to depths of 25 to 42 km. Nodal planes oriented approximately perpendicular to the regional extension direction are steep and coincide with the projections of border faults to the base of the crust. Border faults, therefore, are steep and deep and are the more likely sites of large magnitude earthquakes ( $M > 7$ ). The along-axis structural segmentation of the Tanganyika rift also corresponds to along-axis variations in the seismogenic layer thickness. Existing receiver function data suggest that active magmatic

intrusion may be occurring beneath some rift basins, with rapid stressing causing brittle deformation of ductile lower crust.

#### Acknowledgments

Khalfan Mtelega from the Physics Department of University of Dar-es-Salaam was instrumental in all aspects of the data acquisition program. We thank Seis-UK for the loan of the seismic gear, technical support of the field project, and computing facilities. We also thank Marcus Mn'gong'o and Clement Mndasha from Beach Petroleum for logistical support and generous advice. We are grateful for advice from J. P. O'Donnell and to ThiQuan Pham and Katherine Peterson for assistance with focal mechanism analyses. All data are available on the IRIS DMC (network ZV 2014-2015; <https://ds.iris.edu/SeisQuery/tempNets.phtml>). The facilities of SEIS-UK are supported by the Natural Environment Research Council (NERC) under agreement R8/H10/64. D. K. is supported by NERC grant NE/L013932. F. I. K. is funded through NERC studentship NE/L002531/1, a grant to GSNOC from Roy Franklin O. B.E. and the ECLIPSE program funded by the New Zealand Ministry of Business Innovation and Employment. C. E. acknowledges support of National Science Foundation grant EAR1109302.

#### References

- Abers, G. A. (1991). Possible seismogenic shallow-dipping normal faults in the Woodlark-D'Entrecasteaux extensional province, Papua New Guinea. *Geology*, *19*(12), 1205–1208. [https://doi.org/10.1130/0091-7613\(1991\)019%3C1205:PSSDNF%3E2.3.CO](https://doi.org/10.1130/0091-7613(1991)019%3C1205:PSSDNF%3E2.3.CO)
- Accardo, N. J., Gaherty, J. B., Shillington, D. J., Ebinger, C. J., Nyblade, A. A., Mbofoni, G. J., et al. (2017). Surface wave imaging of the weakly extended Malawi rift from ambient-noise and teleseismic Rayleigh waves from onshore and lake-bottom seismometers. *Geophysical Journal International*, *209*(3), 1892–1905. <https://doi.org/10.1093/gji/ggx133>
- Albaric, J., Déverchère, J., Perrot, J., Jakovlev, A., & Deschamps, A. (2013). Deep crustal earthquakes in North Tanzania, East Africa: Interplay between tectonic and magmatic processes in an incipient rift. *Geochemistry, Geophysics, Geosystems*, *15*, 374–394. <https://doi.org/10.1002/2013GC005027>
- Ambraseys, N. N. (1991). The Rukwa earthquake of 13 December 1910 in East Africa. *Terra Nova*, *3*(2), 202–211. <https://doi.org/10.1111/j.1365-3121.1991.tb00873.x>
- Ambraseys, N. N., & Adams, R. D. (1992). Reappraisal of major African earthquakes, south of 20°N, 1900–1930. *Tectonophysics*, *209*(1–4), 293–296. [https://doi.org/10.1016/0040-1951\(92\)90036-6](https://doi.org/10.1016/0040-1951(92)90036-6)
- Anderson, J. A., & Wood, H. O. (1925). Description and theory of the torsion seismometer. *Bulletin of the Seismological Society of America*, *15*(1), 1–72.
- Axen, G. J. (1992). Pore pressure, stress increase, and fault weakening in low-angle normal faulting. *Journal of Geophysical Research*, *97*(B6), 8979–8991. <https://doi.org/10.1029/92JB00517>
- Barbot, S., Lapusta, N., & Avouac, J.-P. (2012). Under the Hood of the earthquake machine: Toward predictive modeling of the seismic cycle. *Science*, *336*(6082), 707 LP–710. Retrieved from <http://science.sciencemag.org/content/336/6082/707.abstract>
- Boniface, N., & Appel, P. (2018). Neoproterozoic reworking of the Ubendian Belt crust: Implication for an orogenic cycle between the Tanzania Craton and Bangweulu Block during the assembly of Gondwana. *Precambrian Research*, *305*, 358–385. <https://doi.org/10.1016/j.precamres.2017.12.011>
- Borrego, D., Nyblade, A. A., Accardo, N. J., Gaherty, J. B., Ebinger, C. J., Shillington, D. J., et al. (2018). Crustal structure surrounding the northern Malawi rift and beneath the Rungwe Volcanic Province, East Africa. *Geophysical Journal International*, *215*(2), 1410–1426. <https://doi.org/10.1093/gji/ggy331>
- Brazier, R. A., Nyblade, A. A., & Florentin, J. (2005). Focal mechanisms and the stress regime in NE and SW Tanzania, East Africa. *Geophysical Research Letters*, *32*, L14315. <https://doi.org/10.1029/2005GL023156>
- Bufe, C. G., & Varnes, D. J. (1993). Predictive modeling of the seismic cycle of the Greater San Francisco Bay Region. *Journal of Geophysical Research*, *98*(B6), 9871–9883. <https://doi.org/10.1029/93JB00357>
- Camelbeeck, T., & Iranga, M. (1996). Deep crustal earthquakes and active faults along the Rukwa trough, eastern Africa. *Geophysical Journal International*, *124*, 612–630. <https://doi.org/10.1111/j.1365-246X.1996.tb07040.x>
- Chakrabarti, R., Basu, A. R., Santo, A. P., Tedesco, D., & Vaselli, O. (2009). Isotopic and geochemical evidence for a heterogeneous mantle plume origin of the Virunga volcanics, Western rift, East African Rift System. *Chemical Geology*, *259*(3–4), 273–289. <https://doi.org/10.1016/J.CHEMGEO.2008.11.010>
- Cohen, A. S., Soreghan, M. J., & Scholz, C. A. (1993). Estimating the age of formation of lakes: An example from Lake Tanganyika, East African Rift system. *Geology*, *21*(6), 511. [https://doi.org/10.1130/0091-7613\(1993\)021<0511:ETAOFO>2.3.CO;2](https://doi.org/10.1130/0091-7613(1993)021<0511:ETAOFO>2.3.CO;2)
- Condori, C., Tavera, H., Marotta, G. S., Rocha, M. P., & França, G. S. (2017). Calibration of the local magnitude scale ( $M_L$ ) for Peru. *Journal of Seismology*, *21*(4), 987–999. <https://doi.org/10.1007/s10950-017-9647-3>
- Coussement, C., Gente, P., Rolet, J., Tiercelin, J.-J., Wafula, M., & Buku, S. (1994). The North Tanganyika hydrothermal fields, East African Rift system: Their tectonic control and relationship to volcanism and rift segmentation. *Tectonophysics*, *237*(3–4), 155–173. [https://doi.org/10.1016/0040-1951\(94\)90252-6](https://doi.org/10.1016/0040-1951(94)90252-6)
- Craig, T. J., Jackson, J. A., Priestley, K., & McKenzie, D. (2011). Earthquake distribution patterns in Africa: Their relationship to variations in lithospheric and geological structure, and their rheological implications. *Geophysical Journal International*, *185*(1), 403–434. <https://doi.org/10.1111/j.1365-246X.2011.04950.x>
- Delvaux, D. (2001). Tectonic and palaeostress evolution of the Tanganyika-Rukwa-Malawi rift segment, East African rift System. *Peri-Tethys Memoir*, *6*, 545–567.
- Delvaux, D., & Barth, A. (2010). African stress pattern from formal inversion of focal mechanism data. *Tectonophysics*, *482*(1–4), 105–128. <https://doi.org/10.1016/J.TECTO.2009.05.009>
- Delvaux, D., Kervyn, F., Macheyek, A. S., & Temu, E. B. (2012). Geodynamic significance of the TRM segment in the East African Rift (W-Tanzania): Active tectonics and paleostress in the Ufipa plateau and Rukwa basin. *Journal of Structural Geology*, *37*, 161–180. <https://doi.org/10.1016/J.JSG.2012.01.008>
- Déverchère, J., Petit, C., Gileva, N., Radziminovitch, N., Melnikova, V., & San'kov, V. (2001). Depth distribution of earthquakes in the Baikal rift system and its implications for the rheology of the lithosphere. *Geophysical Journal International*, *146*(3), 714–730. <https://doi.org/10.1046/j.0956-540x.2001.1484.484.x>
- Dieterich, J. (1994). A constitutive law for rate of earthquake production and its application to earthquake clustering. *Journal of Geophysical Research*, *99*(B2), 2601–2618. <https://doi.org/10.1029/93JB02581>
- Ebinger, C. J. (1989). Tectonic development of the western branch of the East African Rift System. *Geological Society of America Bulletin*, *101*(7), 885–903. [https://doi.org/10.1130/0016-7606\(1989\)101<0885:TDOTWB>2.3.CO;2](https://doi.org/10.1130/0016-7606(1989)101<0885:TDOTWB>2.3.CO;2)
- Ebinger, C. J., Jackson, J. A., Foster, A. N., & Hayward, N. J. (1999). Extensional basin geometry and the elastic lithosphere. *Philosophical Transactions of the Royal Society of London, Series A: Mathematical, Physical and Engineering Sciences*, *357*(1753), 741 LP–765. Retrieved from <http://rsta.royalsocietypublishing.org/content/357/1753/741.abstract>
- Ebinger, C. J., Karner, G. D., & Weissel, J. K. (1991). Mechanical strength of extended continental lithosphere: Constraints from the Western rift system, East Africa. *Tectonics*, *10*(6), 1239–1256. <https://doi.org/10.1029/91TC00579>
- Ebinger, C. J., Keir, D., Bastow, I. D., Whaler, K. A., Hammond, J. O. S., Ayele, A., et al. (2017). Crustal structure of active deformation zones in Africa: Implications for global crustal processes. *Tectonics*, *36*, 3298–3332. <https://doi.org/10.1002/2017TC004526>
- Ebinger, C. J., & Sleep, N. H. (1998). Cenozoic magmatism throughout East Africa resulting from impact of a single plume. *Nature*, *395*(6704), 788–791. <https://doi.org/10.1038/27417>

- Ekström, G., Nettles, M., & Dziewoński, A. M. (2012). The global CMT project 2004–2010: Centroid-moment tensors for 13,017 earthquakes. *Physics of the Earth and Planetary Interiors*, 200–201, 1–9. <https://doi.org/10.1016/j.pepi.2012.04.002>
- Ellis, M., & King, G. (1991). Structural control of flank volcanism in continental rifts. *Science*, 254(5033), 839 LP–842. Retrieved from <http://science.sciencemag.org/content/254/5033/839.abstract>
- Fishwick, S., & Bastow, I. D. (2011). Towards a better understanding of African topography: A review of passive-source seismic studies of the African crust and upper mantle. *Geological Society, London, Special Publications*, 357(1), 343–371. <https://doi.org/10.1144/sp357.19>
- Foster, A. N., & Jackson, J. A. (1998). Source parameters of large African earthquakes: Implications for crustal rheology and regional kinematics. *Geophysical Journal International*, 134(2), 422–448. <https://doi.org/10.1046/j.1365-246x.1998.00568.x>
- Fréchet, J. (1985). Sismogenèse et doublets sismiques. Thèse d'Etat, Université Scientifique et Médicale de Grenoble, Grenoble, France.
- Fritz, H., Abdelsalam, M., Ali, K. A., Bingen, B., Collins, A. S., Fowler, A. R., et al. (2013). Orogen styles in the East African Orogen: A review of the Neoproterozoic to Cambrian tectonic evolution. *Journal of African Earth Sciences*, 86, 65–106. <https://doi.org/10.1016/j.jafrearsci.2013.06.004>
- Furman, T. (1995). Melting of metasomatized subcontinental lithosphere: Undersaturated mafic lavas from Rungwe, Tanzania. *Contributions to Mineralogy and Petrology*, 122(1–2), 97–115. <https://doi.org/10.1007/s004100050115>
- Got, J.-L., Fréchet, J., & Klein, F. W. (1994). Deep fault plane geometry inferred from multiplet relative relocation beneath the south flank of Kilaua. *Journal of Geophysical Research*, 99(B8), 15,375–15,386. <https://doi.org/10.1029/94JB00577>
- Gutenberg, B., & Richter, C. F. (1954). *Seismicity of the earth and associated phenomena* (2nd ed.). Princeton, NJ: Princeton University Press.
- Halldórsson, S. A., Hilton, D. R., Scarsi, P., Abebe, T., & Hopp, J. (2014). A common mantle plume source beneath the entire East African Rift System revealed by coupled helium-neon systematics. *Geophysical Research Letters*, 41, 2304–2311. <https://doi.org/10.1002/2014GL059424>
- Hardebeck, J. L., & Michael, A. J. (2006). Damped regional-scale stress inversions: Methodology and examples for southern California and the Coalinga aftershock sequence. *Journal of Geophysical Research*, 111, B11310. <https://doi.org/10.1029/2005JB004144>
- Hilbert-Wolf, H. L., Roberts, E. M., & Simpson, E. L. (2016). New sedimentary structures in seismites from SW Tanzania: Evaluating gas- vs. water-escape mechanisms of soft-sediment deformation. *Sedimentary Geology*, 344, 253–262. <https://doi.org/10.1016/j.sedgelo.2016.03.011>
- Hilbert-Wolf, H., Roberts, E., Downie, B., Mtelega, C., Stevens, N. J., & O'Connor, P. (2017). Application of U-Pb detrital zircon geochronology to drill cuttings for age control in hydrocarbon exploration wells: A case study from the Rukwa Rift Basin, Tanzania. *AAPG Bulletin*, 101(2), 143–159. <https://doi.org/10.1306/06281616003>
- Hodgson, I., Illsley-Kemp, F., Gallacher, R. J., Keir, D., Ebinger, C. J., & Mtelega, K. (2017). Crustal structure at a young continental rift: A receiver function study from the Tanganyika rift. *Tectonics*, 36, 2806–2822. <https://doi.org/10.1002/2017TC004477>
- Hutton, L. K., & Boore, D. M. (1987). The  $M_L$  scale in Southern California. *Bulletin of the Seismological Society of America*, 77(6), 2074–2094.
- Illsley-Kemp, F., Keir, D., Bull, J. M., Ayele, A., Hammond, J. O. S., Kendall, J.-M., et al. (2017). Local earthquake magnitude scale and b-value for the Danakil region of northern Afar. *Bulletin of the Seismological Society of America*, 107(2), 521–531. <https://doi.org/10.1785/0120150253>
- Jackson, J., & Blenkinsop, T. (1993). THE Malaŵi earthquake of March 10, 1989: DEep faulting within the East African Rift System. *Tectonics*, 12(5), 1131–1139. <https://doi.org/10.1029/93TC01064>
- Kanamori, H. (1977). The energy release in great earthquakes. *Journal of Geophysical Research*, 82(20), 2981–2987. <https://doi.org/10.1029/JB082i020p02981>
- Kanamori, H. (1983). Magnitude scale and quantification of earthquakes. *Tectonophysics*, 93(3–4), 185–199. [https://doi.org/10.1016/0040-1951\(83\)90273-1](https://doi.org/10.1016/0040-1951(83)90273-1)
- Keir, D., Belachew, M., Ebinger, C. J., Kendall, J.-M., Hammond, J. O. S., Stuart, G. W., et al. (2011). Mapping the evolving strain field during continental breakup from crustal anisotropy in the Afar Depression. *Nature Communications*, 2(1), 285. <https://doi.org/10.1038/ncomms1287>
- Kervyn, F., Ayub, S., Kajara, R., Kanza, E., & Temu, B. (2006). Evidence of recent faulting in the Rukwa rift (West Tanzania) based on radar interferometric DEMs. *Journal of African Earth Sciences*, 44(2), 151–168. <https://doi.org/10.1016/j.jafrearsci.2005.10.008>
- Kissling, E., Kradolfer, U., & Maurer, H. (1995). Program VELEST user's guide—Short introduction. Institute of Geophysics, ETH Zurich.
- Kostrov, V. V. (1974). Seismic moment and energy of earthquakes, and seismic flow of rock. *Physics of the solid earth; Izvestia Akademii nauk SSSR Solid Earth*, 1, 23–44.
- Langston, C. A., Brazier, R., Nyblade, A. A., & Owens, T. J. (1998). Local magnitude scale and seismicity rate for Tanzania, East Africa. *Bulletin of the Seismological Society of America*, 88(3), 712–721.
- Lavier, L. L., & Buck, W. R. (2002). Half graben versus large-offset low-angle normal fault: Importance of keeping cool during normal faulting. *Journal of Geophysical Research*, 107(B6), 2122. <https://doi.org/10.1029/2001JB000513>
- Lindenfeld, M., & Rumpker, G. (2011). Detection of mantle earthquakes beneath the East African Rift. *Geophysical Journal International*, 186(1), 1–5. <https://doi.org/10.1111/j.1365-246X.2011.05048.x>
- Lindenfeld, M., Rumpker, G., Link, K., Koehn, D., & Batte, A. (2012). Fluid-triggered earthquake swarms in the Rwenzori region, East African Rift—Evidence for rift initiation. *Tectonophysics*, 566–567, 95–104. <https://doi.org/10.1016/j.tecto.2012.07.010>
- Lomax, A. (2008). *The NonLinLoc software guide*. Mouans-Sartoux, France: ALomax Scientific. Retrieved from <http://Alomax.Free.Fr/Nlloc>
- Lomax, A., Virieux, J., Volant, P., & Berge-Thierry, C. (2000). Probabilistic earthquake location in 3D and layered models BT—Advances in seismic event location. In C. H. Thurber & N. Rabinowitz (Eds.), (pp. 101–134). Dordrecht: Springer Netherlands. [https://doi.org/10.1007/978-94-015-9536-0\\_5](https://doi.org/10.1007/978-94-015-9536-0_5)
- Martínez-Garzón, P., Kwiatek, G., Ickrath, M., & Bohnhoff, M. (2014). MSATSI: A MATLAB package for stress inversion combining solid classic methodology, a new simplified user-handling, and a visualization tool. *Seismological Research Letters*, 85(4), 896–904. <https://doi.org/10.1785/0220130189>
- Marty, B., Pik, R., & Gezahegn, Y. (1996). Helium isotopic variations in Ethiopian plume lavas: Nature of magmatic sources and limit on lower mantle contribution. *Earth and Planetary Science Letters*, 144(1–2), 223–237. [https://doi.org/10.1016/0012-821X\(96\)00158-6](https://doi.org/10.1016/0012-821X(96)00158-6)
- Mesko, G. T., Class, C., Maqway, M. D., Boniface, N., Manya, S., & Hemming, S. R. (2014). The timing of early magmatism and extension in the Southern East African rift: Tracking geochemical source variability with  $^{40}\text{Ar}/^{39}\text{Ar}$  geochronology at the Rungwe Volcanic Province, SW Tanzania. In *AGU Fall Meeting Abstracts*.
- Morley, C. K. (1988). Variable extension in Lake Tanganyika. *Tectonics*, 7(4), 785–801. <https://doi.org/10.1029/TC007i004p00785>
- Morley, C. K., Cunningham, S. M., Harper, R. M., & Wescott, W. A. (1992). Geology and geophysics of the Rukwa rift, East Africa. *Tectonics*, 11(1), 69–81. <https://doi.org/10.1029/91TC02102>

- Muirhead, J. D., Wright, L. J. M., & Scholz, C. A. (2019). Rift evolution in regions of low magma input in East Africa. *Earth and Planetary Science Letters*, 506, 332–346. <https://doi.org/10.1016/j.epsl.2018.11.004>
- Mulibo, G. D., & Nyblade, A. A. (2013). The P and S wave velocity structure of the mantle beneath eastern Africa and the African superplume anomaly. *Geochemistry, Geophysics, Geosystems*, 14, 2696–2715. <https://doi.org/10.1002/ggge.20150>
- Nyblade, A. A., & Robinson, S. W. (1994). The African Superswell. *Geophysical Research Letters*, 21(9), 765–768. <https://doi.org/10.1029/94GL00631>
- O'Donnell, J. P., Adams, A., Nyblade, A. A., Mulibo, G. D., & Tugume, F. (2013). The uppermost mantle shear wave velocity structure of eastern Africa from Rayleigh wave tomography: Constraints on rift evolution. *Geophysical Journal International*, 194(2), 961–978. <https://doi.org/10.1093/gji/ggt135>
- Richter, C. F. (1935). An instrumental earthquake magnitude scale. *Bulletin of the Seismological Society of America*, 25(1), 1–32.
- Ritsema, J., Nyblade, A. A., Owens, T. J., Langston, C. A., & VanDecar, J. C. (1998). Upper mantle seismic velocity structure beneath Tanzania, East Africa: Implications for the stability of cratonic lithosphere. *Journal of Geophysical Research*, 103(B9), 21,201–21,213. <https://doi.org/10.1029/98JB01274>
- Roberts, E. M., Stevens, N. J., O'Connor, P. M., Dirks, P. H. G. M., Gottfried, M. D., Clyde, W. C., et al. (2012). Initiation of the western branch of the East African rift coeval with the eastern branch. *Nature Geoscience*, 5(4), 289–294. <https://doi.org/10.1038/ngeo1432>
- Rosendahl, B. R., Kilembe, E., & Kaczmarick, K. (1992). Comparison of the Tanganyika, Malawi, Rukwa and Turkana rift zones from analyses of seismic reflection data. *Tectonophysics*, 213(1–2), 235–256. [https://doi.org/10.1016/0040-1951\(92\)90261-4](https://doi.org/10.1016/0040-1951(92)90261-4)
- Saria, E., Calais, E., Stamps, D. S., Delvaux, D., & Hartnady, C. J. H. (2014). Present-day kinematics of the East African Rift. *Journal of Geophysical Research: Solid Earth*, 119, 3584–3600. <https://doi.org/10.1002/2013JB010901>
- Scholz, C. A., & Lyons, R. P. (2010). New age estimates for the Lake Malawi rift, East Africa, using deep scientific drill cores and seismic reflection data. In *AGU Fall Meeting Abstracts*.
- Scholz, C. H. (1968). The frequency-magnitude relation of microfracturing in rock and its relation to earthquakes. *Bulletin of the Seismological Society of America*, 58(1), 399–415.
- Shillington, D. J., Gaherty, J. B., Ebinger, C. J., Scholz, C. A., Selway, K., Nyblade, A. A., et al. (2016). Acquisition of a unique onshore/offshore geophysical and geochemical dataset in the northern Malawi (Nyasa) rift. *Seismological Research Letters*, 87(6), 1406–1416. <https://doi.org/10.1785/0220160112>
- Shudofsky, G. N. (1985). Source mechanisms and focal depths of East African earthquakes using Rayleigh-wave inversion and body-wave modelling. *Geophysical Journal of the Royal Astronomical Society*, 83(3), 563–614. <https://doi.org/10.1111/j.1365-246X.1985.tb04328.x>
- Snoke, J. A. (1984). A program for focal mechanism determination by combined use of polarity and SV-P amplitude ratio data. *Earthquake Notes*, 55, 15.
- Stamps, D. S., Saria, E., & Kreemer, C. (2018). A geodetic strain rate model for the East African Rift System. *Scientific Reports*, 8(1), 732. <https://doi.org/10.1038/s41598-017-19097-w>
- Tarantola, A., & Valette, B. (1982). Generalized nonlinear inverse problems solved using the least squares criterion. *Reviews of Geophysics*, 20(2), 219–232. <https://doi.org/10.1029/RG020i002p00219>
- Tepp, G., Ebinger, C. J., Zal, H., Gallacher, R. J., Accardo, N. J., Shillington, D. J., et al. (2018). Seismic anisotropy of the upper mantle below the Western rift, East Africa. *Journal of Geophysical Research: Solid Earth*, 123, 5644–5660. <https://doi.org/10.1029/2017JB015409>
- Tiercelin, J. J., Chorowicz, J., Bellon, H., Richert, J. P., Mwanbene, J. T., & Walgenwitz, F. (1988). East African rift system: Offset, age and tectonic significance of the Tanganyika-Rukwa-Malawi intracontinental transcurrent fault zone. *Tectonophysics*, 148(3–4), 241–252. [https://doi.org/10.1016/0040-1951\(88\)90133-3](https://doi.org/10.1016/0040-1951(88)90133-3)
- Tongue, J., Maguire, P., & Burton, P. (1994). An earthquake study in the Lake Baringo basin of the central Kenya Rift. *Tectonophysics*, 236(1–4), 151–164. [https://doi.org/10.1016/0040-1951\(94\)90174-0](https://doi.org/10.1016/0040-1951(94)90174-0)
- Tugume, F., Nyblade, A., & Julià, J. (2012). Moho depths and Poisson's ratios of Precambrian crust in East Africa: Evidence for similarities in Archean and Proterozoic crustal structure. *Earth and Planetary Science Letters*, 355–356, 73–81. <https://doi.org/10.1016/j.epsl.2012.08.041>
- Van Der Beek, P., Mbede, E., Andriessen, P., & Delvaux, D. (1998). Denudation history of the Malawi and Rukwa Rift flanks (East African Rift System) from apatite fission track thermochronology. *Journal of African Earth Sciences*, 26(3), 363–385. [https://doi.org/10.1016/S0899-5362\(98\)00021-9](https://doi.org/10.1016/S0899-5362(98)00021-9)
- Vavryčuk, V. (2014). Iterative joint inversion for stress and fault orientations from focal mechanisms. *Geophysical Journal International*, 199(1), 69–77. <https://doi.org/10.1093/gji/ggu224>
- Waldhauser, F. (2001). hypoDD—A program to compute double-difference hypocenter locations (hypoDD version 1.0-03/2001). US Geol. Surv. Open File Rep., 01, 113.
- Wannamaker, P., Hill, G., Stodt, J., Maris, V., Ogawa, Y., Selway, K., et al. (2017). Uplift of the central transantarctic mountains. *Nature Communications*, 8(1), 1588. <https://doi.org/10.1038/s41467-017-01577-2>
- Watts, A., & Burov, E. (2003). Lithospheric strength and its relationship to the elastic and seismogenic layer thickness. *Earth and Planetary Science Letters*, 213(1–2), 113–131. [https://doi.org/10.1016/S0012-821X\(03\)00289-9](https://doi.org/10.1016/S0012-821X(03)00289-9)
- Weeraratne, D. S., Forsyth, D. W., Fischer, K. M., & Nyblade, A. A. (2003). Evidence for an upper mantle plume beneath the Tanzanian craton from Rayleigh wave tomography. *Journal of Geophysical Research*, 108(B9), 2427. <https://doi.org/10.1029/2002JB002273>
- Weinstein, A., Oliva, S. J., Ebinger, C. J., Roecker, S., Tiberi, C., Aman, M., et al. (2017). Fault-magma interactions during early continental rifting: Seismicity of the Magadi-Natron-Manyara basins, Africa. *Geochemistry, Geophysics, Geosystems*, 18, 3662–3686. <https://doi.org/10.1002/2017GC007027>
- Weissel, J. K., & Karner, G. D. (1989). Flexural uplift of rift flanks due to mechanical unloading of the lithosphere during extension. *Journal of Geophysical Research*, 94(B10), 13,919–13,950. <https://doi.org/10.1029/JB094iB10p13919>
- Wesnouslyk, S. G. (2008). Displacement and geometrical characteristics of earthquake surface ruptures: Issues and implications for seismic-hazard analysis and the process of earthquake rupture. *Bulletin of the Seismological Society of America*, 98(4), 1609–1632. <https://doi.org/10.1785/0120070111>
- Woessner, J., & Wiemer, S. (2005). Assessing the quality of earthquake catalogues: Estimating the magnitude of completeness and its uncertainty. *Bulletin of the Seismological Society of America*, 95(2), 684–698. <https://doi.org/10.1785/0120040007>
- Yang, Z., & Chen, W. P. (2010). Earthquakes along the East African Rift System: A multiscale, system-wide perspective. *Journal of Geophysical Research*, 115, B12309. <https://doi.org/10.1029/2009JB006779>